technische universität
dortmund

AWI

Implementation of a Maxwell Elasto-Brittle Rheology in a Sea Ice Model Coupled to an Ocean

Mirjam Aline Bourgett
geboren in Neuwied

2022

Kondensierte Materie - Arbeitsgruppe Kierfeld
Fakultät Physik
Technische Universität Dortmund

Abstract

The viscous-plastic (VP) rheology and the Maxwell elasto-brittle (MEB) rheology were compared in a common framework. To this end, the Massachusetts Institute of Technology general circulation model (MITgcm) was complemented by the MEB rheology for sea ice. The results challenge the reported advantages of the MEB rheology over the VP rheology and encourage further research on the source of spatial heterogeneity in sea ice models.

Kurzfassung

Die viskos-plastische (VP) Rheologie und die Maxwell elasto-brittle (MEB) Rheologie wurden in einem gemeinsamen Simulationsframework miteinander verglichen. Zu diesem Zweck wurde das "Massachusetts Institute of Technology general circulation model" (MITgcm) um die MEB Rheologie erweitert. Die gewonnenen Ergebnisse stellen die vorhergesagten Vorteile der MEB Rheologie in Frage und ermutigen die weitere Untersuchung der Ursache von räumlicher Heterogenität in Meereismodellen.

Acknowledgment

List of Abbreviations

MEB	Maxwell Elasto-Brittle
VP	Viscous-Plastic
EVP	Elastic-Viscous-Plastic
AIDJEX	Arctic Ice Dynamics Joint Experiments
MITgcm	Massachusetts Institute of Technology general circulation model
LKF	Linear Kinematic Feature
IGY	International Geophysical Year
ITD	Ice Thickness Distribution
EB	Elasto-Brittle
MC	Mohr-Coulomb
FV	Finite-Volume
JFNK	Jacobian-Free-Newton-Krylov
LSR	Line-Successive Relaxation
FGMRES	Flexible General Minimum RESidual
IMEX	Implicit-EXplicit

Contents

1 Introduction

Sea ice modelling is an important part of global climate modelling mainly because of the ice-albedo feedback and its effect on the density structure of the ocean. At the same time, sea ice is sensitive to climate warming and can be used as an indicator for the same. In winter, the sea ice protects the warm ocean from the cold atmosphere and in spring and summer, it reflects much of the incoming solar radiation (Hunke et al. 2010). The areal extent, concentration, and thickness of sea ice in Arctic regions effects circulation patterns. Models and observations suggest that a decline of sea ice in the Arctic, together with an increase in snow cover in Eurasia, favours the negative phase of the North Atlantic Oscillation and the Arctic Oscillation (Vihma 2014). Both oscillations influence the weather and climate on global scales.

Sea ice is and has been studied at different scales ranging from micro-scales to scales of thousands of kilometers in order to improve the accuracy of models. While basic large-scale models for either the thermodynamics (Maykut et al. 1971) or dynamics (Hibler 1979) of sea ice have existed for more than 40 years, new models are still being developed. Either new models are being developed to gain more precise descriptions of sea ice's physical processes and characteristics or to extend the existing models with biogeochemical processes (Hunke et al. 2010). Modern sea ice models consider the distribution of sea ice thickness, thermodynamic processes within the ice and its environment, and dynamic processes.

The dynamic processes depend, among other things, on the relation between internal stress and deformation which is called rheology. Until today the commonly used rheology for sea ice is the viscous-plastic rheology (VP). Models using the VP rheology were shown to generate observed statistics of sea ice deformation on large scales. For example, simulated sea ice deformation of a VP model follow a multi-fractal spatial and temporal scaling, as observed from RGPS data (Hutter et al. 2020). However, on small scales, several aspects of the VP models have been discussed to be inconsistent with observations: Weiss et al. (2007) found scaling properties of the modeled sea ice deformation to be in disagreement with observations. Also, they concluded that models such as VP and EVP lack temporal intermittency, in which a small, local perturbation triggers other and larger events while being spatially heterogeneous. The VP model assumptions are based on observations made during the Arctic Ice Dynamics Joint Experiment (AIDJEX) in the 1970s. For example, it was observed that sea ice is strong in compression and weak in tension (no tensile stress allowed). Based on more recent observations, these assumptions have been re-evaluated and found insufficient (Coon et al. 2007). Furthermore, Ringeisen et al. (2019) showed that observed intersection angles between faults in sea ice cannot be simulated with a standard

VP model. Ringeisen et al. results were confirmed by Hutter et al. (2022).

The presented thesis follows the aim to develop more precise descriptions of sea ice's physical processes. Specifically, models on scales of hundred kilometers in space and on scales of hours to a few days in time were used. This study focuses on sea ice dynamics and discusses a not yet commonly used rheology for sea ice: The Maxwell elasto-brittle rheology (MEB). In this thesis, the Massachusetts Institute of Technology general circulation model (MITgcm) (MITgcm Group 2021) was complemented by the MEB rheology for sea ice. This way, a modelling set-up was created to directly compare the already implemented VP and the new MEB rheology in the same numerical framework. Thereby, the results of both rheologies can be analysed and compared in terms of the named inconsistencies between observations and models without other confounding factors such as numerical discretization, advection scheme, and grid resolution.

This thesis starts with a general overview of sea ice modelling, giving a summary of the history of sea ice research (chapter 2) and continuing with a general description of the different parts of a sea ice model (chapter 3). In the next step, the VP rheology and the MEB rheology are explained by introducing the elastic theory of solid, continuous bodies (chapter 4). The implementation of the MEB rheology is presented in chapter 5 as the first part of the results of this thesis and then is tested and compared to already existing results in the following chapters. Firstly, simple analytical solutions of the momentum equation are studied (chapter 6) and secondly, phenomenological tests of simple idealized experiments are analysed (chapter 7). A test for symmetry is presented first, and the results of an idealized ice channel experiment are compared to a MEB implementation in an uncoupled sea ice model (Plante et al. 2020) afterwards. Finally, the newly developed implementation is used for a direct comparison between the results of the VP rheology and the MEB rheology based on the study of Linear Kinematic Features (LKFs) carried out by Mehlmann et al. (2021) (chapter 8). The results challenge previous statements about the advantages of the MEB rheology, specifically, spatial heterogeneity of simulated fields, over the standard VP rheology (Girard et al. 2011).

2 History of Sea Ice Modelling

In the second half of the 20th century, the work on sea ice models started. Discussions on thermodynamic and dynamic processes arose based on observations during the International Geophysical Year (IGY) (1957-1958) and later the AIDJEX (1975-1976). The IGY increased the research in the Arctic and Antarctic polar regions. Afterwards, the AIDJEX program focused on the dynamics of sea ice. In this context, two different ways of treating sea ice were established: a viscous rheology and an elastic-plastic rheology.

The idea to model ice as a viscous fluid was to treat ice in a similar way as water and air and have "some sort of eddy viscosity" (Hibler 1977). In the viscous rheology, the internal ice stress is proportional to the ice deformation rate which makes the computation straightforward. Proponents of the viscous rheology were W. D. Hibler, J. W. Glen, and W. J. Campbell. It was found that results of their models could be used for mean annual ice circulation of the Arctic Ocean (Campbell 1965) and prediction of sea ice dynamics with a lead time of several days (Hibler 1974).

Following further observations made during the AIDJEX program, ice resists compression with fixed stress. This observation contradicts the assumptions of the VP rheology. Also, ice was observed to have little to no resistance to diverging strains once a converging deformation had occurred and stresses behaved independently of the deformation rate.

These observations were the basis for an isotropic, plastic continuum approach: the elastic-plastic rheology. Proponents of this opponent rheology were, for example, M. Coon, R. S. Pritchard, and D. A. Rothrock. In 1974, they formulated, among others, the elastic-plastic rheology for large-scale mechanical behaviour of pack ice (Coon et al. 1974a). The rheology distinguishes between elastic, reversible behaviour for small internal stresses and plastic, irreversible behaviour for stresses beyond a critical stress. Both dynamics were described by separate equations and therefore had to be treated differently. Consequently, one had to keep track of the deformation rate indefinitely to distinguish between both dynamics, which made the rheology numerically and theoretically complex (Hibler 1979). Nevertheless, the elastic-plastic model (Coon et al. 1974a, (p.93-94)) was "designed [...] to include what [was] believed to be the important behavior of the ice".

Combining both, the numerical simplicity of the viscous model with the physical correctness of the elastic-plastic model W. D. Hibler presented his idea of a "Viscous Sea Ice Law as a Stochastic Average of Plasticity" (Hibler 1977), which led to his "Dynamic Thermodynamic Sea Ice Model" (Hibler 1979). W. D. Hibler showed that the viscous constitutive law averaged for small and large deformation rates has a viscous-plastic behaviour. Hence, the plastic behaviour is retained in the VP model and the elastic behaviour was replaced

by a viscous law (Hibler 1979). The implemented MEB sea ice model and the classic VP sea ice model are described in the section on the viscous-plastic rheology (section 4.2). The continuous "Dynamic Thermodynamic Sea Ice Model" and its variants is the basis for almost all sea ice components of global climate models such as the MITgcm.

3 Modern Sea Ice Modelling

Modern sea ice models are used for a wide range of resolutions. To produce operational weather and marine forecasts, resolutions 100 times finer than the ones discussed in the outcomes of the AIDJEX are needed. Short-term sea ice models simulate periods from a few hours to a few days, seasonal models simulate periods over a few month and models which can be used for climate predictions simulate periods over years. The following paragraph follows the book "Sea Ice Analysis and Forecasting" by Carrieres et al. (2017). Starting with the formation of sea ice, the thermodynamics of sea ice growth and melting is essential. Seawater in polar oceans has a freezing point of approximately $-1.8\,°C$ varying with the salinity of the ocean. Sea ice forms needle-shaped ice crystals in seawater around the freezing point. With further cooling, an assembly of these needles forms a layer called grease ice. The grease ice itself forms plates of diameters between tens of centimeters to a few meters when driven closer together by external forces such as wind and waves. Sea ice then grows at the base of this already-formed ice layer depending on the sea ice thickness. The sea ice thickness itself depends not only on the thermodynamic processes but also on dynamic processes. Vice versa, the sea ice thickness influences the thermodynamic growth and the mechanical strength of sea ice which also affects the dynamic processes. There are two common strategies to model ice thickness: Two-Category and Multi-Thickness Category models. Categories in this context mean different states of ice concentration and ice thickness in which an ice thickness distribution (ITD) is discretized. For example, in two-category models, there is only a zero-thickness category for open water and a mean-thickness category for areas covered with ice. Multi-thickness category models usually have between 5 and 10 different categories.

Already formed sea ice influences the ocean around it. During the formation of sea ice the salt contained in sea ice is driven out of the ice so that the seawater around the ice is more saline and hence denser than the rest of the seawater, sinks down and becomes part of a colder and denser layer. The expulsion of salt in the formation process of sea ice is called salt rejection. The sinking of the cold and salty seawater also increases the mixing in the surface layer. The sea ice also has an important effect on the atmosphere above it through modified heat fluxes. A major effect on the atmosphere has the albedo of the ice. The albedo describes the fraction of solar radiation reflected by the sea ice surface. Thereby, the albedo strongly depends on the characteristics of the surface. In this way, sea ice affects the sea or ice surface temperature, which is an essential quantity in large-scale modelling.

The general melting of sea ice consists of the melting processes at the base, the sides,

and the surface of the ice. The conductive heat flux determines the melting at the base through the ice and the ocean heat flux. The open water next to the sea ice has a smaller albedo than the sea ice, absorbs more shortwave radiation, and therefore heats up more and increases the lateral melting in summer. The surface melt of sea ice is also controlled by the albedo.

Nevertheless, the temporal evolution of sea ice depends not only on thermodynamic processes that were shortly described until now, but also on dynamic processes. Dynamic processes are induced by external forcing. The important external forces interacting with ice are wind, Coriolis forcing, and gravitational forcing caused by differences in the sea surface height. All three forcings lead to internal stress within the ice and eventually to the deformation of ice. The relation between internal stress and deformation is called rheology and will be discussed in detail in chapter 4. When it comes to dynamic processes and sea ice movement from one point to another, there are significant implications for the ice-ocean-atmosphere interactions. Sea ice driven by a wind field can create openings. Large openings in an otherwise fully covered ocean are called polynyas. Due to wind forcing, the sea ice can also form leads which are long openings or cracks in the ice shield. These openings of seawater are exposed to the atmosphere directly. This is why in winter, leads and polynyas are preferred locations where new sea ice forms because the ocean is directly exposed to the cold atmosphere an loses heat. The inverse situation can be found in summer. Melting at the sides of polynyas is increased due to the lower albedo. If sea ice is pushed together, so-called pressure ridges can form where either ice is piled up on top of each other or is pushed beneath each other. In both cases, the mean sea ice thickness increases, and the sea ice is more likely to survive summer melting.

Sea ice modelling attempts to parameterize all the aforementioned properties and more detailed features. To do that, sea ice models use equations based on four fundamental laws: the conservation of momentum, the conservation of mass, the conservation of energy and the conservation of salt. For the implementation of the new MEB rheology, the momentum equation is of the highest interest.

Momentum equation   The thickness of sea ice ($\mathcal{O}(1\,\mathrm{m})$) is much smaller than the horizontal scales of motion ($\mathcal{O}(100\,\mathrm{m}\text{-}1000\,\mathrm{km})$), so that vertical variations of sea ice properties are not important for sea ice dynamics. Hence, sea ice momentum equations are vertically integrated leading to the following 2D equations of the horizontal momentum:

$$m\frac{\mathrm{d}\boldsymbol{u}}{\mathrm{d}t} = -\hat{z} \times m f_c \boldsymbol{u} + a\boldsymbol{\tau_a} + a\boldsymbol{\tau_w} + \boldsymbol{\nabla} \cdot \boldsymbol{\sigma} - mg\nabla H_0 \tag{3.1}$$

where m is the mass per area, $\boldsymbol{u} = u\hat{x} + v\hat{y}$ is the horizontal velocity vector with the unit vectors $\hat{x}$ and $\hat{y}$ and the velocity in x-direction u and the velocity in y-direction v. Furthermore, f_c is the Coriolis parameter, a is the sea ice concentration, and $\boldsymbol{\tau_a}$ and $\boldsymbol{\tau_w}$ are wind and water stress. The divergence of the stress tensor $\nabla \cdot \boldsymbol{\sigma}$ is called rheology term,

g is the gravity acceleration parameter and H_0 is the sea surface height. In the case of sea ice, the stress terms and the rheology term dominate the ice dynamic. The typical horizontal velocity of sea ice is between 0 to $1\,\text{m/s}$. Depending on the ice concentration in an area, the external forcing increases the internal stresses. In areas with higher ice concentrations, the rheology term dominates the dynamics. When the ice concentration is low, the interaction between ice floes can be neglected, the rheology term is small, and the ice is in "free drift". The rheology itself is represented by the constitutive equation and describes how sea ice reacts to external forcing as well as other stresses.

Constitutive equation   This equation describes the relation between stress σ and deformation ε. In general, sea ice can resist some external forcing without permanent deformation, but there is a critical value above which sea ice deformation starts. For different rheologies, there are different constitutive equations. As mentioned in chapter 2, most sea ice models use a viscous-plastic rheology based on Hibler (1977). Chapter 4 treats the elastic theory of solid materials and discusses the VP rheology and the new MEB rheology in detail.

Characteristics of the deformation of sea ice   The behaviour described with the constitutive equation follows observations of sea ice. As mentioned in chapter 2, the AIDJEX found ice to resist compression with a fixed stress and to have little to no resistance to diverging strains once a converging deformation had occurred. More recent observations also observed the mechanism of fracturing and the subsequent deformation in more detail. Weiss et al. (2007) analysed in-situ ice stress data, satellite-derived ice strain rates and laboratory observations and found the strain rate not to be proportional to the stress. Instead, they observed inelastic deformations for all spatial and time scales, even under small stresses, and therefore, higher strain rates than assumed by models. Sea ice exhibits temporal intermittency where a small, local perturbation can trigger other and larger events while being spatially heterogeneous. For example, linear kinematic features (LKFs) can form. These are areas where the deformation is highly localized, and the velocity gradient is spatially discontinuous as it is the case for leads and ridges. Following this, Coon et al. (2007) stated that an accurate sea ice model has to directly account for discontinuities in the velocity field due to the opening and closing of leads and allow anisotropic behaviour. Intersection angles of deformation patterns observed via Landsat, Seasat/SAR, and areal photographs, AVHRR emerged in the range of $(15 \pm 2)°$ at scales from $100\,\text{m}$ to $100\,\text{km}$ (Erlingsson 1988).

A detailed description of the numerical implementation of these equations is presented in chapter 5, specifically for the MITgcm framework.

4 Rheologies in Sea Ice Models

This chapter outlines the elastic theory of solid materials and discusses the VP rheology and the new MEB rheology in detail.

4.1 Elastic Theory

Many terms and equations of the elastic theory can be used to describe the 2D ice layer. In the case of the MEB rheology, the brittle part is added to a continuous model. Also, many sea ice rheologies assume the ice behaves elastically up to a certain level of stress. Therefore, the basis for the VP and MEB rheology is the elastic theory that covers the mechanics of solid, continuous bodies.

Continuous bodies deform under stress. The deformation $\Delta x_i = x_i' - x_i$ per unit length x_i (with $x_1 = x, x_2 = y, x_3 = z$) is the strain ε_i. In a 2D material, there can be uniaxial and biaxial strains. All strains can be described by a strain tensor ε_{ik} which can be written for small deformations as

$$\varepsilon_{ik} = \frac{1}{2} \left(\frac{\partial \Delta x_i}{\partial x_k} + \frac{\partial \Delta x_k}{\partial x_i} \right) \tag{4.1}$$

(Landau et al. 1989, chapter 1) with $i, k \in [1, 2]$.

The stress component is vertically integrated over the ice thickness to model stress in the whole ice sheet. Consequently, the unit of stress is Nm^{-1}. The stress acting on the 2D layer can be described by four stress components: two normal stresses (σ_{11}, σ_{22}) acting perpendicular to the surface and two shear stresses (σ_{12}, σ_{21}) acting tangential to the surface (see Figure 4.1). The stress tensor is symmetric ($\sigma_{12} = \sigma_{21}$) in a system without rotational forces. To be coherent with the later used sign convention for stress, normal stresses in the negative x or y direction are tensile stresses, and normal stresses in the opposite direction are compressive stresses.

Following Landau et al. (1989), the linear dependency between stress and strain allows deriving the stress tensor from the strain tensor and vice versa for isotropic, solid bodies. In 3D, the classical elastic constitutive equation is called *generalized Hook's law* and consists of nine equations expressing the stress components as linear homogeneous functions of the strain components. For an elastical isotropic material, in which no direction is preferred, the constitutive equation is

$$\sigma_{ij} = \Lambda \varepsilon_{kk} \delta_{ij} + 2M \varepsilon_{ij} \tag{4.2}$$

with Λ and M being the Lamé elastic constants and δ_{ij} the Kronecker delta (Malvern 1969, chapter 6). The Lamé elastic constants can be written in terms of the elastic modulus E, the shear modulus G and Poisson's ration ν

$$M = G = \frac{E}{2(1 + \nu)} \quad \text{and} \quad \Lambda = \frac{\nu E}{(1 + \nu)(1 - 2\nu)} \tag{4.3}$$

(Malvern 1969, chapter 6). The elastic modulus E is the proportionality factor for the normal stress-strain relation along the same axis. *Poisson's ratio* gives the ratio of the perpendicular strain to the strain in the direction of the stress

$$\nu = \frac{\varepsilon_{11}}{\varepsilon_{22}}, \tag{4.4}$$

here for stress acting in y -direction (Landau et al. 1989, chapter 1). The proportionality factor for the shear stress-strain relation is the shear modulus G.

The generalized Hooke's law can be written in matrix form. In 2D, using the plane stress assumption, the matrix form is

$$\begin{pmatrix} \sigma_{11} \\ \sigma_{22} \\ \sigma_{12} \end{pmatrix} = EC \begin{pmatrix} \varepsilon_{11} \\ \varepsilon_{22} \\ \varepsilon_{12} \end{pmatrix} \tag{4.5}$$

with

$$C = \begin{pmatrix} C_{11} & C_{12} & C_{13} \\ C_{21} & C_{22} & C_{23} \\ C_{31} & C_{32} & C_{33} \end{pmatrix} \tag{4.6}$$

and

$$C_{11} = C_{22} = \frac{1}{1 - \nu^2},$$
$$C_{12} = C_{21} = \frac{\nu}{1 - \nu^2},$$
$$C_{33} = \frac{(1 - \nu)}{1 - \nu^2} \text{ ,and}$$
$$C_{13} = C_{23} = C_{31} = C_{32} = 0$$

(Malvern 1969, chapter 6). Following Malvern 1969 (chapter 3) the stress state can also be described with the eigenvalues, the principal stresses σ_1 and σ_2, of the stress matrix. In the coordinate system of the principal stresses, the normal stresses are extremal, and
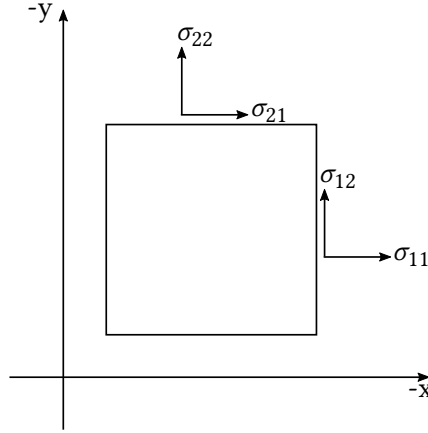
Figure 4.1: The four stress components in a 2D plane. Two normal stresses (σ_{11}, σ_{22}) and two shear stresses (σ_{12}, σ_{21}).

there is no shear stress. The principal stresses are

$$
\begin{aligned}
\sigma_1 &= \frac{\sigma_{11} + \sigma_{22}}{2} + \sqrt{\left(\frac{\sigma_{11} - \sigma_{22}}{2}\right)^2 + \sigma_{12}^2}, \\
\sigma_2 &= \frac{\sigma_{11} + \sigma_{22}}{2} - \sqrt{\left(\frac{\sigma_{11} - \sigma_{22}}{2}\right)^2 + \sigma_{12}^2}.
\end{aligned}
\tag{4.7}
$$

The principal stresses can describe a circle, *Mohr's circle*, where the same stress states in a material are on the circle. Mohr's circle exists in the invariant stress plane with the center

$$
Z = \left(\frac{\sigma_{11} + \sigma_{22}}{2}, 0\right)
\tag{4.8}
$$

and the radius

$$
r = \sqrt{\left(\frac{\sigma_{11} - \sigma_{22}}{2}\right)^2 + \sigma_{12}^2}.
\tag{4.9}
$$

The center Z and the radius r are the invariants σ_I and σ_{II} with

$$
\begin{aligned}
\sigma_I &= \frac{\sigma_{11} + \sigma_{22}}{2} \\
\sigma_{II} &= \sqrt{\left(\frac{\sigma_{11} - \sigma_{22}}{2}\right)^2 + \sigma_{12}^2}.
\end{aligned}
\tag{4.10}
$$

The invariant σ_I is used to describe the divergent part of stress, and the invariant σ_{II} to describe the shear stress.

In addition to *Hookean solids*, where the stress depends upon strain, there is a second category for continuous bodies: *The ideal Newtonian fluid*. The stress in ideal Newtonian fluids depends upon the rate of deformation

$$\dot{\varepsilon}_{ik} = \frac{1}{2} \left(\frac{\partial \Delta u_i}{\partial x_k} + \frac{\partial \Delta u_k}{\partial x_i} \right) \tag{4.11}$$

with the velocity vector $\boldsymbol{u}$. Invariant deformation rates $\dot{\varepsilon}_I$ and $\dot{\varepsilon}_{II}$ can be defined analogously to the invariant stresses (4.10) as

$$\begin{aligned} \dot{\varepsilon}_I &= \dot{\varepsilon}_{11} + \dot{\varepsilon}_{22} \\ \dot{\varepsilon}_{II} &= \sqrt{\left(\dot{\varepsilon}_{11} - \dot{\varepsilon}_{22} \right)^2 + 4\dot{\varepsilon}_{12}^2}. \end{aligned} \tag{4.12}$$

In contrast to solids, a fluid cannot support shear stresses. This means that shear deformation occurs in fluids as long as a shear stress is exerted. As mentioned, the viscous constitutive equation

$$\sigma_{ij} = 2\eta\dot{\varepsilon}_{ij} \tag{4.13}$$

shows a linear dependency between stress σ_{ij} and strain rate $\dot{\varepsilon}_{ij}$ with the viscosity η (Malvern 1969, chapter 6). Unlike elastic materials, viscous materials do not have a memory of its initial state, and the stress at a point only depends on the instantaneous rate of deformation at that point. Viscous dynamics are not reversible as elastic dynamics.

The third category of dynamics within a body is plastic deformation. In the case of plastic deformation, the relation between the stress and the strain is non-linear and the deformation is irreversible (Malvern 1969, chapter 6).

In both of the following rheologies, stress states define the deformation of the ice. There are stress states in which the ice behaves elastically or viscously and stress states in which the ice deforms plastically. Yield criteria are used to describe the transition from one (dynamic) state to another. The yield criteria for both VP and MEB rheology are pictured in Figure 4.2 in both invariant (black) and principal (gray) stress states. Within the yield curve, the material behaves like an elastic or viscous material. Once one yield criterium is reached, the material deforms plastically.

4.2 Viscous-Plastic Rheology

The rheology used in many sea ice models is the VP rheology. The original model was introduced by Hibler (1979). In the following VP rheology, the "ice interacts in a rigid-plastic manner for normal deformation rates and as a linear viscous fluid, with a pressure term, for small deformation rates" (Hibler 1979, p. 817). Furthermore, the maximum compressive stress P depends on the ice thickness h and the sea ice concentration a.

The transition between viscous and plastic treatment is defined with an elliptical yield curve (Figure 4.2). The elliptic yield curve describes a 2D rigid plastic law and can be expressed as

$$F(\sigma_1, \sigma_2) = \left(\frac{\sigma_1 + \sigma_2 + P}{P}\right)^2 + \left(\frac{\sigma_2 - \sigma_1}{P}e\right)^2 - 1 = 0 \tag{4.14}$$

with $P = 2a$ being the length of the ellipse's major axis and the ratio of the two semi-major axes is $e = a/b$. The ellipse is centered at $(-P/2, -P/2)$. In this way, P is the maximum compressive stress. From the ellipse equation (4.14), an explicit expression for the stress σ_{ij} in dependency of the strain rate $\dot{\varepsilon}_{ij}$ can be derived by using the associated flow rule for plastic deformations on the ellipse

$$\dot{\varepsilon}_{ij} = \gamma \frac{\partial F}{\partial \sigma_{ij}}. \tag{4.15}$$

with γ being a function of the strain rate. γ can be derived by combining Equation 4.14 and Equation 4.15 (Hibler 1977). The constitutive equation follows as

$$\sigma_{ij} = 2\eta \dot{\varepsilon}_{ij} + \left[(\zeta - \eta)\dot{\varepsilon}_{kk} - \frac{P}{2}\right]\delta_{ij} \tag{4.16}$$

with

$$\zeta = \frac{P}{2\Delta},$$

$$\eta = \frac{P}{2\Delta e^2},$$

$$\Delta = \sqrt{(\dot{\varepsilon}_{11} + \dot{\varepsilon}_{22})^2 + ((\dot{\varepsilon}_{11} - \dot{\varepsilon}_{22})^2 + 4\dot{\varepsilon}_{12}^2)\frac{1}{e^2}}$$

(Hibler 1977). Within the VP rheology, it is distinguished between the shear viscosity η and the bulk viscosity ζ. In all other chapters, η is the viscosity. The parameter Δ rewritten in terms of the strain rate invariants (4.12)

$$\Delta = \sqrt{\dot{\varepsilon}_I^2 + \frac{1}{e^2}\dot{\varepsilon}_{II}^2}, \tag{4.17}$$

shows the dependency of the viscosities ζ and η on the strain rate $\dot{\varepsilon}_{ij}$ and the maximum compressive stress P. The dependency of ζ, η, $\dot{\varepsilon}_{ij}$, and P is chosen in a way that the stress

states lie on the elliptical yield curve (Hibler 1979). Both viscosities ζ and η become arbitrarily large for small strain rates because $\Delta \to 0$. Consequently, the viscosities ζ and η are limited from above by setting a minimum $\Delta_{\min}$. Once Equation 4.17 is smaller than the minimum $\Delta_{\min}$, Δ is set to $\Delta_{\min}$ and is not dependent on the strain rate anymore. Hence, the dynamic follows a linear viscous law and the stress states lie in the inside of the ellipse. Also, a limiting value for the maximum compressive stress state, depending on the ice strength, is set. This way, stress states inside the ellipse behave in a viscous manner and stress states on the ellipse in a plastic manner.

The maximum compressive stress P is coupled to the ice strength parameter P^*, the sea ice thickness h and the sea ice concentration a

$$P = P^* h \mathrm{e}^{-C^*(1-a)} \tag{4.18}$$

with the free parameter C^* (Hibler 1979).

Hibler (1979) stated that his model considers sea ice to be on average isotropic on large scales, the effective tensile strength to be low for all strain rates, the stress states to be relatively independent of the strain rate magnitude, and the sea ice to exhibit large compressive strength under convergence.

Apart from the elliptic yield curve, a circular yield curve was suggested by Coon et al. (1974a), and a teardrop-shaped yield curve was used by Coon et al. (1974b). Recently, yield curves, such as the Coulombic yield curve which allows tensile stresses, have been tested. The Coulombic yield curve was introduced by Hibler et al. (2000) and consists of an ellipse shifted towards tensile stresses, which is truncated comparable to the *Mohr-Colomb* (MC) yield curve shown in Figure 4.2 which is used with the MEB rheology. For example, Ringeisen et al. (2019) compared intersection angles between faults using the standard elliptic yield curve and a Coulombic yield curve. The intersection angles calculated with the Coulombic yield curve grossly matched the observations in contrast to the ones calculated with the elliptic yield curve which could not match the observations. The critical constants of a VP sea ice model are the ice strength parameter P^*, the ratio of the semi-major axes of the yield curve e and the free parameter C^*. In Hibler (1977), it was suggested to set the shear viscosity η smaller than the bulk viscosity ζ. Therefore, $e = 2$ is chosen in many VP models. The free parameter C^* is set to 20 so that the 10 % of open water have a substantial impact on the sea ice strength (diminished by a factor e^{-2}) (Hibler 1979). The ice strength P^* itself is a free parameter, which was adjusted to fit observed and predicted ice drifts. In Hibler (1979), the ice strength was set to $P^* = 5 \times 10^3$ N/m. Later paper chose the ice strength parameter up to 25 times bigger (Tran et al. 2015). In this thesis, the ice strength or the compressive strength in MEB is set to 27.5×10^3 N/m following Ringeisen et al. (2019), Dumont et al. (2009) and others.

4.3 Maxwell Elasto-brittle Rheology

The MEB rheology was invented as an alternative to the commonly used VP rheology. After observations of the strain rate and the fracturing processes within ice either by in-situ measurements, satellite data or laboratory experiments carried out by Weiss et al. (2007) and others, Girard et al. (2011, p. 123) found the VP rheology to be "not suited to describe the multi-scale fracturing processes that accommodate sea-ice deformation".
The VP model was found to be inadequate to model long-range elastic interactions and to reproduce scaling properties and temporal intermittency compared to observations (Weiss et al. 2007). Based on those findings, Girard et al. (2011) proposed an elasto-brittle (EB) rheology, in which the sea ice is treated as a continuous elastic plate with implemented damage, which allows to trigger avalanches of damage. The EB rheology was used for rock mechanics before. It was shown that the EB rheology could give better results than the VP rheology for the distribution of strain rates and the scaling laws in a sea ice model (Girard et al. 2011).
Dansereau et al. (2016) developed the MEB rheology based on the EB rheology. The main adaptation was the extension of the constitutive equation with a viscous-like relaxation term and the coupling of both mechanical parameters to the brittle damage. The viscous part describes the dissipation of the elastic strains into permanent deformation. The reason for the adaptation, Dansereau et al. (2016) argued, is the lack of representation of the permanent deformations following damaging events. In the EB rheology, reversible and irreversible deformations cannot be solved separately. Consequently, the actual ice drift has to be calculated by making assumptions on the reversible and irreversible parts of the deformation, which were calculated simultaneously. The MEB rheology can be understood as a simple connection in series of a viscous damper and an elastic spring

$$\boldsymbol{\sigma} + \frac{\eta}{E}\,\dot{\boldsymbol{\sigma}} = \eta f(\dot{\boldsymbol{\epsilon}}) \tag{4.19}$$

with the stress tensor $\boldsymbol{\sigma}$ and a function of the strain rate tensor $f(\dot{\boldsymbol{\epsilon}})$. In detail, the aim of the MEB rheology is to use a completely isotropic rheology that reproduces the anisotropy and extreme gradients within the ice based only on the constitutive equation and not by treating discontinuities within the velocity field explicitly. The following description of the MEB rheology follows Dansereau et al. (2016). The MEB rheology consists of a linear elastic part of the constitutive equation for a continuous solid, a viscous part of the constitutive equation for irreversible deformations, a local *Mohr Coulomb* (MC) criterium for brittle failure and an isotropic progressive damage mechanism that rescales the viscous and elastic dynamics to initiate avalanches of damage. A healing mechanism to counteract the effect of the damage can be added.
The constitutive equation for a 2D compressible, elastic, continuous solid follows from Equation 4.19 as

$$\dot{\boldsymbol{\sigma}} + \lambda(t)^{-1}\boldsymbol{\sigma} = E(\delta)[\boldsymbol{C}:\dot{\boldsymbol{\epsilon}}] \tag{4.20}$$

with

$$\lambda(t)^{-1} = \frac{E(\delta)}{\eta(\delta)},$$

the elastic modulus tensor C in Equation 4.6 and

$$[C : \dot{\varepsilon}] = \begin{pmatrix} C_{11} & C_{12} & C_{13} \\ C_{21} & C_{22} & C_{23} \\ C_{31} & C_{32} & C_{33} \end{pmatrix} \cdot \begin{pmatrix} \dot{\varepsilon}_{11} \\ \dot{\varepsilon}_{22} \\ \dot{\varepsilon}_{12} \end{pmatrix}. \tag{4.21}$$

Both parameters E and η depend on the integrity parameter δ. Because of different definitions of damage in literature, the integrity δ is used following the definition of damage by Dansereau et al. (2016). The integrity is a scalar parameter equal to 1 for undamaged ice and 0 for entirely damaged ice. A damage parameter d is introduced to describe damaging events which is $d = 1 - \delta$. The relative positions of the stress states to the critical stress values on the yield curve define δ. The yield curve used for the MEB rheology is the MC criterion and is pictured in Figure 4.2. In the principal stress plane and with the convention of compressive stresses being positive, the MC criterion is

$$\sigma_1 = q\sigma_2 + \sigma_c \tag{4.22}$$

where q is the slope of the envelope defined by the internal friction coefficient μ as

$$q = \left((\mu^2 + 1)^{1/2} + \mu \right)^2. \tag{4.23}$$

The critical uniaxial compressive stress σ_c, the intersection of the MC criterion with the σ_1 axis (see Figure 4.2), is

$$\sigma_c = 2c\sqrt{q} \tag{4.24}$$

where c is the cohesion. In contrast to the elliptic yield curve, this yield curve permits tensile stresses, and Dansereau et al. (2016) introduce an extended MC criterion. The critical tensile stress is defined as the intersection of the σ_2 axis with the MC criterion so that

$$\sigma_t = -\frac{\sigma_c}{q} \tag{4.25}$$

(see Figure 4.2). Damaging occurs when stress states exceed the yield curve. Contrary to the VP yield curve, the stress states exceed the yield curve, and there is no normal flow rule on the yield curve. Instead, the distance to the yield curve d_{crit} (called the critical damage) is calculated for each stress component and the maximum distance is taken

$$d_{\text{crit}} = \min\left[1, \frac{\sigma_t}{\sigma_2}, \frac{\sigma_c}{\sigma_1 - q\sigma_2} \right]. \tag{4.26}$$

The critical damage d_{crit} is used to set the stress back onto the yield curve and to update δ. The stress before the correction $\boldsymbol{\sigma'}$ is set back onto the yield curve as following

$$\boldsymbol{\sigma} = d_{\text{crit}} \cdot \boldsymbol{\sigma'}. \tag{4.27}$$

The integrity δ is supposed to contain the history of previous damaging events, so the time evolution is a simple relaxation and is defined as

$$\frac{\partial \delta}{\partial t} = \frac{d_{\text{crit}} - 1}{T_d} \delta + \frac{1}{T_h} \tag{4.28}$$

on a timescale T_d. Healing can be included by choosing a healing time T_h on time scales of the damage time T_d. Additionally, the mechanical parameters are scaled with δ

$$E(t) = E^0 \delta(t) = f_1(E^0, \delta) \tag{4.29}$$

$$\eta(t) = \eta^0 \delta(t)^\alpha = f_2(\eta^0, \delta) \tag{4.30}$$

with $0 < \delta(t = 0) \leq 1$ so that the relaxation parameter is

$$\lambda(t) = \frac{\eta^0}{E^0} \delta(t)^{\alpha-1}, \tag{4.31}$$

with η^0 and E^0 being the mechanical parameters without damage and α a constant greater than 1. This means that within an undamaged ice cover, the viscosity η is very large, the relaxation parameter increases, the viscous term in Equation 4.20 is negligible, and deformations are strictly elastic. Along highly damaged zones, the elastic modulus E vanishes, the relaxation parameter decreases, and most stress leads to permanent deformations. Furthermore, a local drop in E can cause a redistribution in stress so that the damage propagates through the medium. The viscosity η and the elastic modulus E are coupled to the ice concentration a in the same way the ice strength parameter P^* within the VP rheology:

$$E = f_1(E^0, \delta) e^{C^*(1-a)} \tag{4.32}$$

$$\eta = f_2(\eta^0, \delta) e^{C^*(1-a)} \tag{4.33}$$

with $f_1(E^0, \delta)$ and $f_2(\eta^0, \delta)$ representing the functional dependency on the level of damage of the mechanical parameter E^0 and η^0.

For a discretization in space and in time, the MEB implementation follows, for the most parts, Plante et al. (2020) and is introduced in chapter 5 in detail.

For the simulation, the model parameters are chosen to match the physical observations of sea ice. Dansereau et al. (2016) suggest setting the internal friction coefficient μ to 0.7 following observations (eg. Schulson et al. 2006). The undamaged elastic modulus E^0 can be calculated from the elastic shear wave propagation speed $c_w = 500\,\text{m/s}$ and the ice

density $\rho = 900\,\mathrm{kg/m^3}$ to $E^0 = 2c_w^2(1+\nu)\rho = 5.58 \times 10^8$ Pa. Timco et al. (2010) recommend $E^0 = 10 \times 10^9$ Pa for the undamaged elastic modulus. The undamaged viscosity η^0 can be set to $1 \times 10^7 \cdot E^0$ Pa s (Dansereau et al. 2016). Dansereau et al. 2016 also suggest a value between 25×10^3 Pa and 50×10^3 Pa for the ice cohesion c and propose to use noise in the spatial distribution of the cohesion.

The *Courant–Friedrichs–Lewy* condition has to be considered for the timescale parameter for damage T_d. The parameterization of the damage is sensitive to the model time step Δt. Therefore, Dansereau et al. (2016) chose $T_d = \Delta t$, so that the damage does not travel faster than elastic waves within the ice. Plante et al. (2020) go further and propose a damage time $T_d < \Delta t$.

Other implementations and adaptions of the MEB rheology followed Dansereau et al. (2016) and Plante et al. (2020). For example, Rampal et al. (2016) implemented a Lagrangian sea ice model called neXtSIM using the MEB rheology. They state that the neXtSIM model can simulate sea ice over a wide range of spatial and temporal scales in good agreement with observational data. However, the implementation itself differs significantly from the presented implementation of the MEB rheology since a Lagrangian method is used instead of a finite-volume method. Olason et al. (2022) on the other hand, adapted the MEB rheology and used a *Birmingham-Maxwell* constitutive law. In both cases, the models represent the scaling properties of sea ice in time and space (Rampal et al. 2016 and Olason et al. 2022).

4.4 Cohesive Material
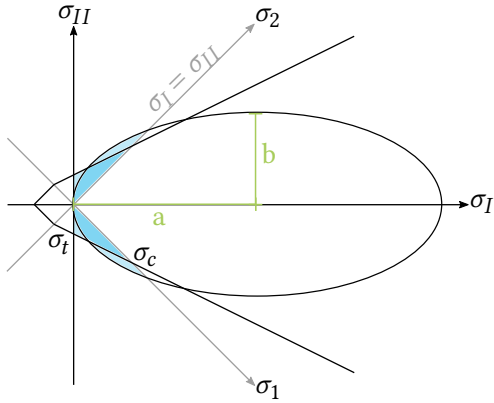
Figure 4.2: Illustration of elliptic yield curve (VP) and yield curve with tensile stresses (MEB). Invariant stress axes (σ_I, σ_{II}) in black and principal stress axes (σ_1, σ_2) in grey. σ_t is the critical tensile stress and σ_c is the uniaxial compressive stress. *a* and *b* denote the semi-major axes of the elliptic yield curve. Cohesive stress states in both rheologies are marked blue.

A material is cohesive if it can sustain uni-axial stresses either in tension and/or compression. In the stress plane, the yield curve of such material touches or even crosses the principle stress axes. In terms of the Mohr-Coulomb theory, this is true for $\sigma_I < |\sigma_{II}|$. For the VP and the MEB rheology, this is marked by blue shading in Figure 4.2. In the case of the VP elliptic yield curve, the cohesion *c* of the simulated ice increases by increasing *b*. Consequently, decreasing the ratio of the two semi-major axes *e* has the same effect. The ice strength parameter P^* can also control the cohesion *c*. In the case of the MEB rheology, the cohesion *c* is its specific input parameter and controls the slope of the yield curve. A higher cohesion and also a higher ice concentration leads to a higher resistance of the ice. Walker (1966) found cohesive material to allow higher shear stresses and thereby to be able to create a self-obstruction to flow within restricted environments such as hoppers, channel, and tubes. For small-scale ice channel experiments, Ip (1993) found that ice arching is only possible for rheologies with cohesive strength. Following Plante et al. (2020) the cohesion *c* is treated constant in space if not stated otherwise. Girard et al. (2011) and Dansereau et al. (2017) used a variable cohesion parameter *c* that is randomly drawn from a uniform distribution to account for faults and cracks on the subgrid scale.

5 The MITgcm Framework

All work presented was computed with the Massachusetts Institute of Technology general circulation model (MITgcm Group 2021). The MITgcm is a general circulation model used to study the atmosphere, the ocean, and the climate. It is discretized with a finite volume discretization on an Arakawa C-grid (Adcroft et al. 2004). The sea ice model is coupled to the ocean model and inherits the horizontal discretization and grid of the ocean model (Losch et al. 2010). The surface stresses are computed from the atmospheric state and are modified by the ice model at every time step. No-slip and free-slip lateral boundary conditions are possible with the FV C-grid code (Losch et al. 2010). The MITgcm framework and a documentation can be found at https://mitgcm.org.

The thermodynamic modules, including the treatment of the conservation of salt and conservation of energy, are not used for the idealized experiments. Also, the module in which healing of sea ice is included, is, for now, not coupled to the thermodynamics. The healing evolves only with the damage parametrisation using a constant healing rate.

The momentum equations are derived from the conservation of momentum. The general momentum equation (3.1) contains terms for the Coriolis deflection, the wind-ice and ocean ice-stresses, a term for the gravity acceleration and a rheology term. To simplify the equation for the following discussions, all terms which are linear in the velocity $\boldsymbol{u}$ and the ice-ocean stress term are summed up in one variable $\boldsymbol{F}$ and the momentum equation follows as

$$m\frac{\partial \boldsymbol{u}}{\partial t} = \nabla \cdot \boldsymbol{\sigma} + \boldsymbol{F}. \tag{5.1}$$

The presented discretization closely follows the implementation presented in Plante et al. (2020). To solve the momentum equation (5.1), the stress $\boldsymbol{\sigma}$ needs to be expressed in terms of the constitutive equation (4.20) which itself depends on the velocity $\boldsymbol{u}$. This is why a semi-implicit backward Euler scheme is used to discretize the constitutive equation

$$\sigma_{ij}'^n = \frac{\Delta t}{1 + \frac{\Delta t}{\lambda^n}} E^n \left[C : \dot{\boldsymbol{\varepsilon}}^n \right] + \frac{1}{1 + \frac{\Delta t}{\lambda^n}} \sigma_{ij}^{n-1} \tag{5.2}$$

with n denoting the variables are calculated in the present time step and $n - 1$ denoting the variables were calculated in the previous time step. Thereby, σ_{ij}^{n-1} is a stress memory term. $\boldsymbol{\sigma}'$ is the stress state before applying a correction required to ensure that the stress state lies within the yield curve (Equation 4.27). The semi-implicit backward Euler scheme is only a minor modification to the standard Euler approximation (Cromer 1981).

19

Putting Equation 5.2 into the momentum equation (5.1) and using the components of the elastic modulus tensor (4.6) leads to

$$m\frac{u^n - u^{n-1}}{\Delta t} = \frac{\partial}{\partial x}(\chi^{n-1}C_{11}\dot{\varepsilon}_{xx}^n) + \frac{\partial}{\partial x}(\chi^{n-1}C_{12}\dot{\varepsilon}_{yy}^n) + \frac{\partial}{\partial y}(\chi^{n-1}C_{33}\dot{\varepsilon}_{xy}^n)$$

$$+ \frac{\partial}{\partial x}\left(\frac{\chi^{n-1}}{E^{n-1}\Delta t}\sigma_{xx}^{n-1}\right) + \frac{\partial}{\partial y}\left(\frac{\chi^{n-1}}{E^{n-1}\Delta t}\sigma_{xy}^{n-1}\right) + F_x^n \tag{5.3}$$

$$m\frac{v^n - v^{n-1}}{\Delta t} = \frac{\partial}{\partial y}(\chi^{n-1}C_{11}\dot{\varepsilon}_{yy}^n) + \frac{\partial}{\partial y}(\chi^{n-1}C_{21}\dot{\varepsilon}_{xx}^n) + \frac{\partial}{\partial x}(\chi^{n-1}C_{33}\dot{\varepsilon}_{xy}^n)$$

$$+ \frac{\partial}{\partial y}\left(\frac{\chi^{n-1}}{E^{n-1}\Delta t}\sigma_{yy}^{n-1}\right) + \frac{\partial}{\partial x}\left(\frac{\chi^{n-1}}{E^{n-1}\Delta t}\sigma_{xy}^{n-1}\right) + F_y^n \tag{5.4}$$

with $\chi^{n-1} = \frac{E^{n-1}\Delta t}{1+\Delta t/\lambda^{n-1}}$. An implicit backward Euler method is used for the time discretization of the integrity parameter δ, so that

$$\delta^n = \delta^{n-1}\left(\frac{\Delta t}{T_d}(d_{\text{crit}}^n - 1) + 1\right) + \frac{\Delta t}{T_h}. \tag{5.5}$$

It is essential to mention that the integrity δ is calculated multiple times within one time step. The details follow in the algorithm shown in (algorithm 1).

When implementing the discretized momentum equation (5.4) and the discretized integrity (5.5), two aspects must be considered. First of all, a similarity with the constitutive equation of the VP rheology can be used to decrease the number of code changes. Most of the VP code can be used by re-interpreting model variables. Secondly, the numerical stability of the solution depends on how often variables are averaged from one point on the grid to another point. Averaging becomes necessary when variables defined at the center of the grid (C-point) and on the corner of the grid (Z-point) are used in the same calculation. Starting with the similarity to the VP constitutive equation (4.16), the elastic part of the constitutive equation of the MEB rheology, the first term in (5.2), can be rewritten as

$$[C : \dot{\varepsilon}]_{ij} = \frac{v}{(1+v)(1-v)}\dot{\varepsilon}_{kk}\delta_{ij} + \frac{1}{1+v}\dot{\varepsilon}_{ij}$$

$$= 2\frac{1-v}{2(1-v^2)}\dot{\varepsilon}_{ij} + \left[\left(\frac{v+1}{2(1-v^2)} - \frac{1-v}{2(1-v^2)}\right)\dot{\varepsilon}_{ij} - \frac{0}{2}\right]\delta_{ij}$$

$$= 2\frac{C_{22}}{2}\dot{\varepsilon}_{ij} + \left[\left(\frac{C_{11}+C_{12}}{2} - \frac{C_{22}}{2}\right)\dot{\varepsilon}_{ij} - \frac{0}{2}\right]\delta_{ij}. \tag{5.6}$$

Therefore, the already existing VP code with $\eta = \frac{C_{22}}{2}$ and $\zeta = \frac{C_{11}+C_{12}}{2}$ can be used to implement the elastic part of the stress (5.6).

The different parameters in the momentum equation (5.4) are defined at different grid

points in the MITgcm framework. Scalars such as the ice thickness h, the ice concentration A, the relaxation parameter λ, and the elastic modulus E are originally defined at C-points. The vector field of the sea ice velocity $\boldsymbol{u}$ is defined at the sides of the grid cell. With finite differences on the C-grid the diagonal terms of the strain rate tensor $\dot{\varepsilon}_{xx}$ and $\dot{\varepsilon}_{yy}$ are naturally defined at C-points

$$(\dot{\varepsilon}_{xx})_{ij}^C = \frac{u_{i+1,j} - u_{i,j}}{\Delta x_{i,j}^F},\tag{5.7}$$

$$(\dot{\varepsilon}_{yy})_{ij}^C = \frac{v_{i,j+1} - v_{i,j}}{\Delta y_{i,j}^F},\tag{5.8}$$

and the off-diagonal components $\dot{\varepsilon}_{xy}$ at Z-points

$$(\dot{\varepsilon}_{xy})_{ij}^Z = \frac{1}{2}\left(\frac{v_{i,j} - v_{i-1,j}}{\Delta x_{i,j}^v} + \frac{u_{i,j} - u_{i,j-1}}{\Delta y_{i,j}^u}\right).\tag{5.9}$$

In the case of an equidistant, squared C-grid, all distances between velocity components are the same ($\Delta x_{i,j}^F = \Delta y_{i,j}^F = \Delta x_{i,j}^v = \Delta y_{i,j}^u$). Consequently, the tensor fields of the strain rate $\dot{\varepsilon}$ and of the stress tensor σ are defined at the C- and Z-points. The main diagonal components ($\dot{\varepsilon}_{xx}$, $\dot{\varepsilon}_{yy}$, σ_{xx}, σ_{yy}) are located at C-points and off-diagonal components ($\dot{\varepsilon}_{xy}$, σ_{xy}) at Z-points. Each time a variable defined at a C-point has to be computed in the same operation as a variable defined at a Z-point, one of the two has to be averaged to the other one's position. For example, the MC criterion (4.22) to calculate the critical damage d_{crit} uses all three stress components which are defined at C and Z-points

$$\begin{aligned}\sigma_{c,C} = {}& \frac{\sigma_{11,C} + \sigma_{22,C}}{2} + \sqrt{\left(\frac{\sigma_{11,C} + \sigma_{22,C}}{2}\right)^2 + \sigma_{12,Z}^2}\\&- q_C\frac{\sigma_{11,C} + \sigma_{22,C}}{2} - \sqrt{\left(\frac{\sigma_{11,C} - \sigma_{22,C}}{2}\right)^2 + \sigma_{12,Z}^2}\,.\end{aligned}\tag{5.10}$$

To calculate the critical stress $\sigma_{c,C}$ at C-points the shear stress component σ_{12} has to be averaged from Z- to C-points. These averaging operations lead to numerical instabilities. Averaging variables from C- to Z-points and vice versa can lead to a computational mode. This computational mode carries no spatial information. Consequently, two averaged variables can evolve independently of each other because they are decoupled. When decoupled variables lead to independent solutions the resulting field can exhibit a checkerboard instability. A solution of the problem is to define some variables on both C- and Z-points and also to have the least averaging operations possible. Using variables from which many other variables can be computed, reduces the number of averaging further.

With this in mind, different combinations of variable definitions at both grid points were

compared. The following variables showed the least numerical instabilities and are defined at both C- and Z points: the shear stress σ_{12}, the critical damage d_{crit} and the integrity δ, the relaxation parameter λ, and the shear viscosity η. Moreover, in some cases it was possible to define the second parameter at the other grid point without the need of averaging. In this way, the number of averaging operations was reduced to three.

Both d_{crit} and d are defined as scalars originally at C-points. To calculate d_{crit} (4.26) at C-points, the shear stress σ_{12} needs to be available at C-points. Instead of averaging the shear stress component σ_{12} from Z-points to C-points each time the critical damage d_{crit} is averaged, a second shear stress at C-points $\sigma_{12,\text{C}}$ is defined. Following Equation 5.2, the shear strain rate component $\dot{\varepsilon}_{xy}$ needs to be averaged from Z-points to C-points to calculate the shear stress component $\sigma_{12,\text{C}}$. In this way, the shear stress at C-points $\sigma_{12,\text{C}}$ evolves without coupling to the shear stress at Z-points and the shear strain rate is averaged instead of the shear stress. Many other combinations of averaging were tried in the course of this thesis, but this method proved to be the only stable one. The same was observed for the shear stresses in Plante et al. (2020). This is one of the three averaging operations. Next, the original shear stress component σ_{12} is defined on Z-points and all scalars used in Equation 5.2 need to be available at Z-points. However, only the integrity parameter δ needs to be averaged from C-points to Z-points because the other parameters are derived from it. After obtaining δ_Z by averaging δ, the relaxation parameter on Z-points λ_Z and the shear viscosity on Z-points η_Z can be recomputed from δ_Z. This is the second averaging operation.

Lastly, the critical damage d_{crit} needs to be available on Z-points to correct the shear stress component $\sigma_{12,Z}$. This is the third averaging operation.

In this thesis, all averaging operations from C-points to Z-points are done by a linear average

$$\alpha_{ij,Z} = \frac{1}{4} \left(\alpha_{ij,\text{C}} + \alpha_{i+1j,\text{C}} + \alpha_{ij+1,\text{C}} + \alpha_{i+1j+1,\text{C}} \right) \tag{5.11}$$

and a quadratic average is used to average from Z-points to C-points

$$\alpha_{ij,\text{C}} = \sqrt{\frac{1}{4} \left(\alpha_{ij,Z}^2 + \alpha_{i+1j,Z}^2 + \alpha_{ij+1,Z}^2 + \alpha_{i+1j+1,Z}^2 \right)}. \tag{5.12}$$

5.1 Iterative Solver

In the MITgcm framework, several different solver options are implemented. For this thesis, a *Jacobian-Free-Newton-Krylov* (JFNK) solver (Losch et al. 2014) is used for the VP simulations and a *Picard* solver with a matrix-free *Krylov* solver (Lemieux et al. 2008) is used for the simulations with the MEB rheology.

Starting with the solver for the MEB rheology, a standard *Picard* solver using a line-successive-relaxation (LSR) (Losch et al. 2010) is adapted with a *Krylov* solver using a

Flexible General Minimum RESidual (FGMRES) to solve the nonlinear system of the momentum equation (5.4). The integrity parameter δ is additionally calculated using an IMplicit-EXplicit (IMEX) approach (Lemieux et al. 2014). The algorithm is described in algorithm 1. Each time step n, values of the ocean and the atmospheric model, such as the surface tilt and the wind forcing, are passed to the ice model. The nonlinear momentum equation is then solved in an iterative scheme. In the Picard solver, the nonlinear equations are linearized and solved using a preconditioned FGMRES. The LSR is used to precondition the equation. The FGMRES is a Krylov method which uses the Krylov subspace to solve the linear equation in Equation 5.4 of the form $A(\boldsymbol{u}_{i-1}) \cdot \boldsymbol{u}_i - \boldsymbol{b}_{i-1} = 0$ without the need to find the inverse $A(\boldsymbol{u}_{i-1})^{-1}$. The Picard iteration is repeated until the residual error is reduced by a factor of 1×10^{-4}. The integrity δ, the critical damage d_{crit}, and the elasticity E are calculated based on the recent solution of the velocity $\boldsymbol{u}_i$ each Picard iteration. After the Picard iteration, the stress state is corrected by the latest critical damage and stored as the stress memory for the next step. The same happens with δ. Differing from Plante et al. (2020), only the integrity δ and the elasticity E are included and recalculated in the IMEX scheme.

The JFNK solver is used to solve the nonlinear system of equation of the momentum equations for the VP rheology as described in Losch et al. (2014). In each time step, the nonlinear system of equations is solved implicitly. An inexact Newton method is used, where the linear system is solved with an accuracy depending on the nonlinear convergence rate. Again, LSR is used as a preconditioner and the inverse of the Jacobian matrix is calculated with the matrix-free Krylov solver using FGMRES.

The JFNK solver could not be used for the MEB rheology because it requires continuous (differentiable) solutions, but the damage scheme of the MEB rheology introduces discontinuities by the definition of the critical damage d_{crit} (4.26).

Algorithm 1 MEB solver

---

1. Receive values from the atmosphere and ocean
2. Start nonlinear Picard iteration $\boldsymbol{u}^{n-1} \rightarrow \boldsymbol{u}_0$
while $i < i_{max}$ & not converged **do**
    2.1 $i = i + 1$
    2.2 Calculate external stresses $\boldsymbol{\tau}_i$
    2.3 Calculate strain rates $\dot{\boldsymbol{\varepsilon}}_i$
    2.4 Calculate viscosities η_{i-1}, ζ_{i-1} and relaxation parameter λ_{i-1}
    2.5 Calculate $b\left(\boldsymbol{u}_{i-1}\right)$
    2.6 Calculate $A\left(\boldsymbol{u}_{i-1}\right)\boldsymbol{u}_i$
    2.7 Initial residual
    2.8 Krylov loop
    while not converged **do**
        2.8.1 Calculate $\boldsymbol{u}_i$ by solving the linear system with FGMRES
    end while
    2.9 Calculate damage criterion $d_{crit,i}$ and damage parameter d_i (IMEX)
    2.10 Calculate elasticity E_i
end while
3. $\boldsymbol{u}_i \rightarrow \boldsymbol{u}^n$
4. $d_i \rightarrow d^n$
5. $d_{crit,i} \rightarrow d^n_{\text{crit}}$
6. $E_i \rightarrow E^n$
7. Update stress to yield curve $\boldsymbol{\sigma}^n = d^n_{\text{crit}} \cdot \boldsymbol{\sigma}'^n$

---

6 Simple Analytical Solutions

(a) Wind vertical to boundaries in the x-direction.   **(b)** Wind along boundaries in the y-direction.
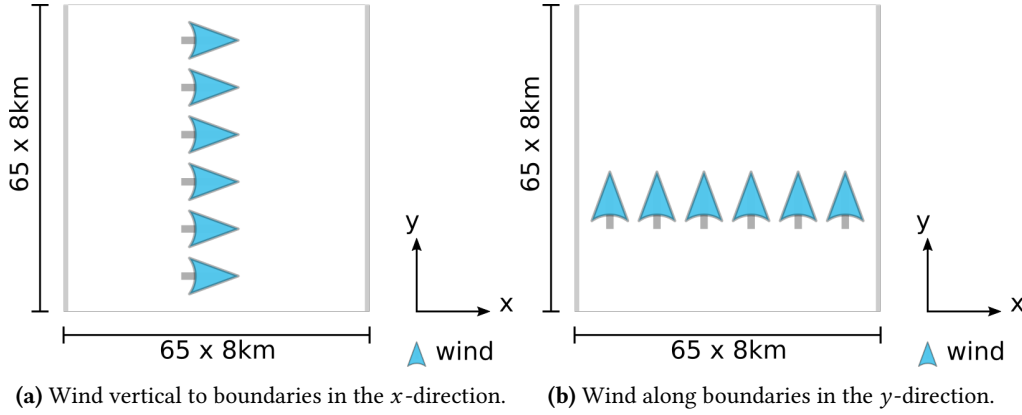
Figure 6.1: Ice channel along y-axis to recreate steady state solutions.

In the first step of testing the new implementation, model results are compared with analytic solutions. For the analytic solutions, sea ice in an infinite channel along the y-direction on a non-rotating plane is considered. The momentum equation (5.1) in 1D for steady state ($\boldsymbol{u} = 0$) simplifies to

$$\frac{\partial \sigma_{xx}}{\partial x} + \tau_x = 0 \tag{6.1}$$

and

$$\frac{\partial \sigma_{xy}}{\partial x} + \tau_y = 0 \tag{6.2}$$

only considering external wind forcings along the x- and y-axis. Derivatives in y-direction $(\partial/\partial y)$ can be neglected due to symmetry in translation of the experiment.

The normal stress component σ_{xx} can be obtained by integrating Equation 6.1 over the channel width in the x-direction x for external wind forcing only along the x-axis

$$\sigma_{xx}(x) = -\tau_x \cdot x. \tag{6.3}$$

The normal stress component σ_{yy} results in

$$\sigma_{yy}(x) = -v \cdot \sigma_{xx}(x) \tag{6.4}$$

following Possion's ration (4.4). Since the shear stress σ_{xy} is zero due to zero forcing in the y-direction τ_y, the stress invariants are

$$\sigma_I(x) = \frac{\sigma_{xx}(x)(1+v)}{2} \quad \text{and} \quad \sigma_{II}(x) = \frac{\sigma_{xx}(x)(1-v)}{2}. \tag{6.5}$$

The analytic value for external wind forcing of $5\,\text{m/s}$ for the divergent stress σ_I at the channel walls ($x = \pm W$) results in

$$\sigma_I(\pm W) = \pm 6286.8\,\frac{\text{N}}{\text{m}} \tag{6.6}$$

and for the shear stress σ_{II} in

$$\sigma_{II}(\pm W) = 3385.2\,\frac{\text{N}}{\text{m}} \tag{6.7}$$

by using the values for air density ρ_a and air drag coefficient C_a as stated in Table 7.1.

In the second case with wind forcing along the y-axis, the normal stress components σ_{xx} and σ_{yy} are zero because $\tau_x = 0$. Therefore, only the shear stress component σ_{xy} defines the invariant stresses σ_I and σ_{II}. For the shear stress component σ_{xy}, Equation 6.2 is integrated over the channel width in x-direction x

$$\sigma_{xy}(x) = -\tau_y \cdot x. \tag{6.8}$$

So that the invariant stresses are

$$\sigma_I(x) = 0 \quad \text{and} \quad \sigma_{II}(x) = |\sigma_{12}|. \tag{6.9}$$

In this set-up, the analytic values for an external forcing of $5\,\text{m/s}$ and the same air density and air drag coefficient lead to a divergent stress σ_I at the channel walls of

$$\sigma_I(\pm W) = 0.0\,\frac{\text{N}}{\text{m}} \tag{6.10}$$

and a shear stress σ_{II} of

$$\sigma_{II}(\pm W) = 9672.0\,\frac{\text{N}}{\text{m}}. \tag{6.11}$$

The idealized experiment is set up according to Figure 6.1, and the model parameters can be found in Table 7.1. The model domain is a (512 x 512) km basin closed at the boundary in the West and East and with periodic boundary conditions in the North and South. The domain is covered by 30 cm of ice. The grid cell width Δx is 8 km leading to 64 grid cells in the x-direction with an additional "dry" grid cell to form the solid boundaries in the East and West.

The results of the simulations can be found in Figure 6.2 and Figure 6.3. To reproduce the idealized assumptions made for the analytical results, the simulation needs to be in steady state. Therefore, the damage update has to be set to 0 so that Equation 6.1 and Equation 6.2 are solved. To find a steady state, the domain-mean values for the divergent and shear stress over time were compared (see graphics a) in Figure 6.2 and Figure 6.3). Because the divergent stress has both negative and positive values equally distributed, only in this specific case of a closed channel, the mean of the absolute divergent stress values $\overline{|\sigma_I|}$ are investigated.

In both cases of external forcing, a steady state was found in which the values varied with a relative deviation in orders of 1×10^{-5} or below. The steady state was reached after 14 416 s. In the experiment in which the wind direction is across the channel, an elastic oscillation can be seen for the adjustment process before reaching the steady state for both domain-mean stresses. Whereas, in the experiment in which the wind direction is along the channel, the elastic oscillation can only be observed for the mean shear stress since the mean divergent stress is zero.

In graphics b) (Figure 6.2, Figure 6.3), stress fields in a steady state are shown. The theoretically predicted stress along the x-axis can be observed in both wind directions. The theoretical equations of the stress along the x-axis in Equation 6.5 are compared to the marked transects in the center of the channel in both stress fields. The comparison is shown in c) respectively.

The results for wind in the x-direction show the linear decay for the divergent stress σ_I and the triangular devolution for the shear stress σ_{II}. The results for the divergent stress at the channel walls ($x = \pm W$) are

$$\sigma_I(-W) = -6282.7 \, \frac{\text{N}}{\text{m}} \quad \text{and} \quad \sigma_I(+W) = 6284.7 \, \frac{\text{N}}{\text{m}} \tag{6.12}$$

and for the shear stress

$$\sigma_{II}(-W) = 3383.0 \, \frac{\text{N}}{\text{m}} \quad \text{and} \quad \sigma_{II}(+W) = 3384.1 \, \frac{\text{N}}{\text{m}}. \tag{6.13}$$

The results for wind in the y-direction show no divergent stress σ_I as foreseen since the ice is uniformly accelerated along the boundary in the West. Moreover, the same triangular devolution for the shear stress σ_{II} can be observed as with the wind in the x-direction. The results for the divergent stress at the channel walls ($x = \pm W$) are

$$\sigma_I(-W) = 0.0 \, \frac{\text{N}}{\text{m}} \quad \text{and} \quad \sigma_I(+W) = 0.0 \, \frac{\text{N}}{\text{m}} \tag{6.14}$$

and for the shear stress

$$\sigma_{II}(-W) = 9679.9 \, \frac{\text{N}}{\text{m}} \quad \text{and} \quad \sigma_{II}(+W) = 9679.9 \, \frac{\text{N}}{\text{m}}. \tag{6.15}$$

The highest relative deviation from the theoretical value to the modelled one is the value for the shear stress σ_{II} with forcing along the channel which deviates by 0.08 % from the theoretical value. All in all, the model shows the predicted analytic behaviour and reproduces it nearly exactly in both wind directions and for both invariant stresses. Consequently, the test yields confidence in the new implementation and shows that the averaging between variables of stress does not trigger noise and the new MEB implementation can reproduce the analytic predictions on this scale and with this time resolution.
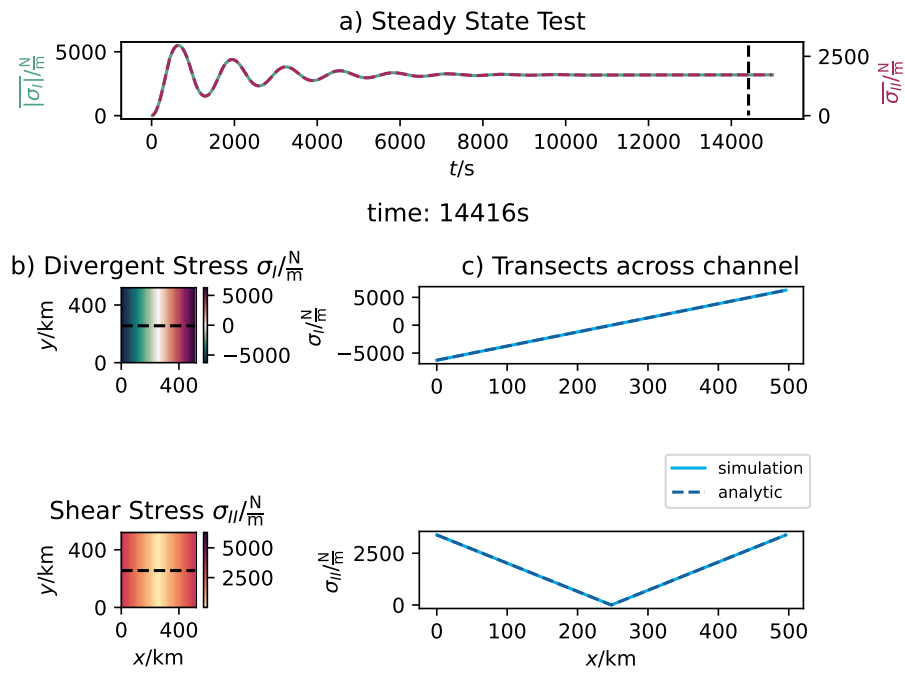
Figure 6.2: Invariant stress analysis in channel along the y-axis with forcing in the x-direction. Plot a) is the time evolution of the domain-mean stress invariant $\overline{|\sigma_I|}$ in green and $\overline{\sigma_{II}}$ in red. In b) there are snapshots of the stress invariants (σ_I, σ_{II}) after reaching the steady state. The dashed black line indicates the transect taken for the plots c). In c) the transects of the simulated stress invariants (σ_I, σ_{II}) are light blue and the analytic prediction are dark blue dashed lines.
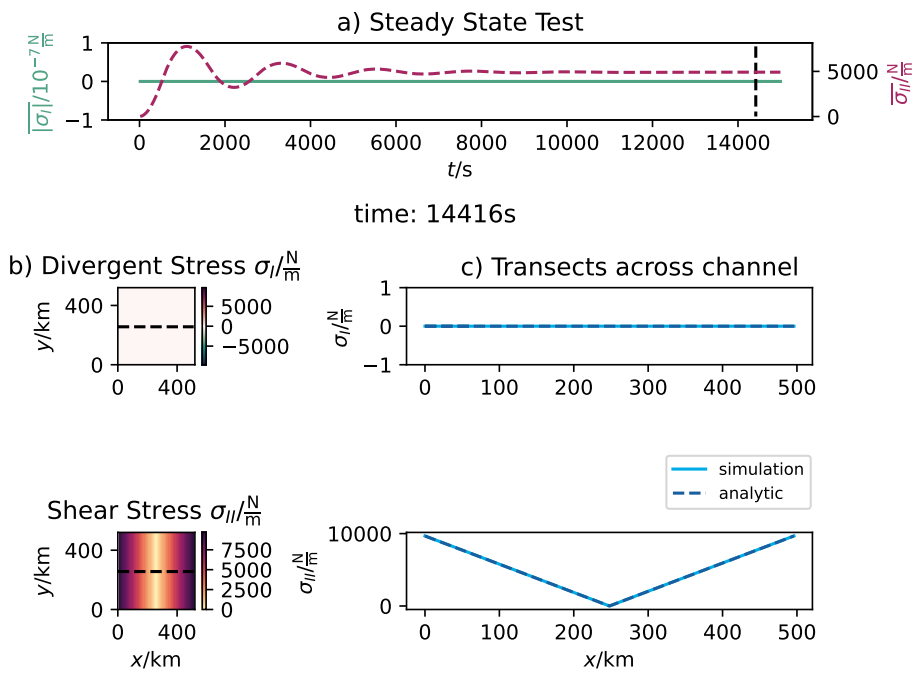
Figure 6.3: Invariant stress analysis in channel along the y-axis with forcing in the y-direction. Plot a) is the time evolution of the domain-mean stress invariant $\overline{|\sigma_I|}$ in green and $\overline{\sigma_{II}}$ in red. In b) there are snapshots of the stress invariants (σ_I, σ_{II}) after reaching the steady state. The dashed black line indicates the transect taken for the plots c). In c) the transects of the simulated stress invariants (σ_I, σ_{II}) are light blue and the analytic prediction are dark blue dashed lines.

7 Phenomenological Testing

The following chapter sums up phenomenological tests to show the elementary behaviour of the implemented rheology. Two idealized experimental set-ups were tested. Both experiments have only external wind forcing, neglecting the Coriolis deflection.
First, the implementation is tested for simple symmetry in an experiment with symmetric geometry and forcing. Secondly, the results of a reference run used in Plante et al. (2020) are compared with the results of the MEB implementation of the MITgcm.
The analysis focuses on the fracturing of ice. Fracturing has a timescale of seconds, which is well below thermodynamic timescales, so healing processes can be neglected for these tests. The corresponding model parameters for each test can be found in Table 7.1.

Table 7.1: Model parameters of the test set-ups. The parameters for the symmetry test on the left and the parameters of the channel test to compare with the reference run (Plante et al. 2020) on the right.

Parameter	Definition	Symmetry test	Channel test	Unit
Δx	Spatial resolution	8	2	km
Δt	Time step	4	0.5	s
t_d	Damage time	16	2	s
E_0	Elastic modulus	5×10^8	1×10^9	N/m
ν	Poisson ratio	0.3	0.3	
λ_0	Viscous relaxation	1×10^7	1×10^5	N s/m
μ	Internal friction	0.7	0.71	
c_0	Cohesion	25×10^3	10×10^3	N/m
ρ_a	Air density	1.3	1.3	$1/m^3$
ρ_i	Sea ice density	9×10^2	9×10^2	$1/m^3$
ρ_w	Water density	1.026×10^3	1.026×10^3	$1/m^3$
C_a	Air drag coefficient	1.2×10^{-3}	1.2×10^{-3}	
C_w	Water drag coefficient	5.5×10^{-3}	5.5×10^{-3}	

7.1 Symmetry

(a) Wind in x-direction. **(b)** Wind in y-direction. **(c)** Wind along diagonal axis.
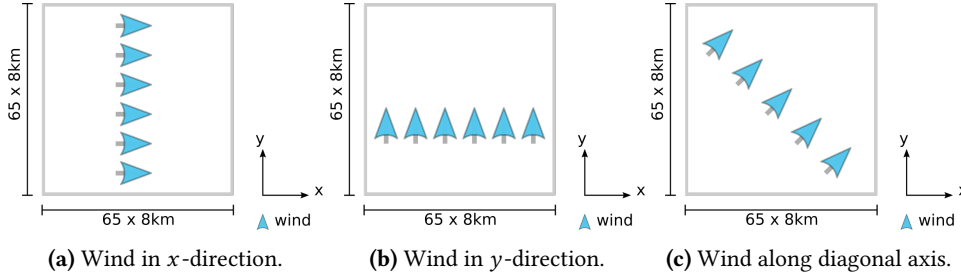
Figure 7.1: Illustrations of set-ups to test for symmetry with different external wind forcing direction.

The model domain is a (512 x 512) km closed basin covered by 30 cm of ice. The grid cell width Δx is 8 km leading to 64 grid cells in each direction with additional "dry" grid cells to form the solid boundaries (see Figure 7.1).

Turning off all external forcings in the quadratic experiment, except for wind forcing, allows testing the implementation for symmetry along the axis of wind forcing. The symmetry is measured by the variance of the asymmetry of speed with respect to the horizontal (h), vertical (v) or diagonal (d) axis:

$$\beta(s_{\text{asym}})^k = \frac{\sum_{i,j}\left(s_{ij} - s_{ij}^k\right)^2}{N} \tag{7.1}$$

with $k \in [\text{h}, \text{v}, \text{d}]$, s_{ij} the field of speed along the axis k, s_{ij}^k the field of speed reflected at the axis k, N the total of grid points in the domain and i, j giving the position in the domain. For the wind in the x-direction (Figure 7.1a), reflection symmetry with respect to the horizontal axis is expected until the non-linear processes, caused by damaging events, dominate the ice dynamics.

The variance of the asymmetry $\beta(s_{\text{asym}})^h$ of speed with respect to the horizontal axis shows exactly this (green) (Figure 7.2). The asymmetry for the first 4500 s of the simulation is negligibly small and increases in response to a second strong increase in damage (dark blue) (Figure 7.2).

In the case of external forcing along the y-axis, reflection symmetry with respect to the vertical axis is expected and the simulation is expected to behave identically with wind in the x- and the y-direction. No difference in the evolution of damage means no preference for one axis.

The asymmetry $\beta(s_{\text{asym}})^v$ is small for the first 4500 s but the asymmetry increases after the damage increased substantially (green) (Figure 7.3). Moreover, the behaviour of the model is different for the two different forcing directions. Although, the evolution of the damage shows no major difference between the wind in the x- or in the y-direction, a difference in

the model between the wind directions becomes visible with the variances of asymmetric speed $\beta(s_{\text{asym}})^h$, $\beta(s_{\text{asym}})^v$. So the general behaviour of the damage is as expected, but the differences between wind in the x- and the y-directions indicate a remaining issue with the numerical stability.

The differences in the variance in speed $\beta(s_{\text{asym}})^h$, $\beta(s_{\text{asym}})^v$ were examined for systematic errors because of the unequal increase of the variance. This is done by comparing the evolution of the difference between the speed field for wind in the x-direction and the speed field for wind in the y-direction. The difference in both fields did not appear in the first 10 timesteps and increased randomly on a very small scale later. With this result, a systematic error can be excluded. The reason for the resulting different behaviour is attributed to numerical instabilities which increase asymmetry in the output field with increasing damage. Increasing asymmetry with increasing damaging events could also be observed in the second test (section 7.2) and hint at a numerically unstable damage parametrisation.

As a second symmetry test, the same procedure was repeated with wind forcing in a diagonal direction in the positive x- and y-direction (see Figure 7.1c). The absolute speed of wind is the same ($|\boldsymbol{u}| = 10\,\text{m/s}$). No difference in the variance of speed $\beta(s_{\text{asym}})^d$ above 1×10^{-7} develops. There is no asymmetry in contrast to the first symmetry test with wind forcings aligned with the grid in the x- or y-direction.

This can be explained with overall fewer damaging events because fewer stress states reach the yield curve. The damage does not reach a value of $d = 0.25$ while the damage in the experiment with the wind blowing in the x- or y-direction significantly exceeds $d = 0.4$. Damage is mainly triggered by the failure of the ice in tensile stress or shear stress (cf. MC-yield curve in Figure 4.2). With wind along the diagonal, compressive stress in the north-eastern corner, tensile stress in the south-western corner and shear stress along the eastern and northern boundary forms (not shown). Only the tensile stress in the south-western corner essentially contributes to the damaging of the ice. The shear stress does not cause damage because the grid cells with high values in shear stress have high values in compressive stress at the same time and the critical value for shear stress rises with increasing compressive stress (cf. MC-yield curve in Figure 4.2).

The absence of asymmetry with small damage values in the case of diagonal wind forcing confirms that the parametrisation of damage is one reason for numerical instabilities. Consequently, all three results show negligible asymmetry for the first 2000 s of the test and the appearing asymmetry follows the expectations of being triggered by damage.
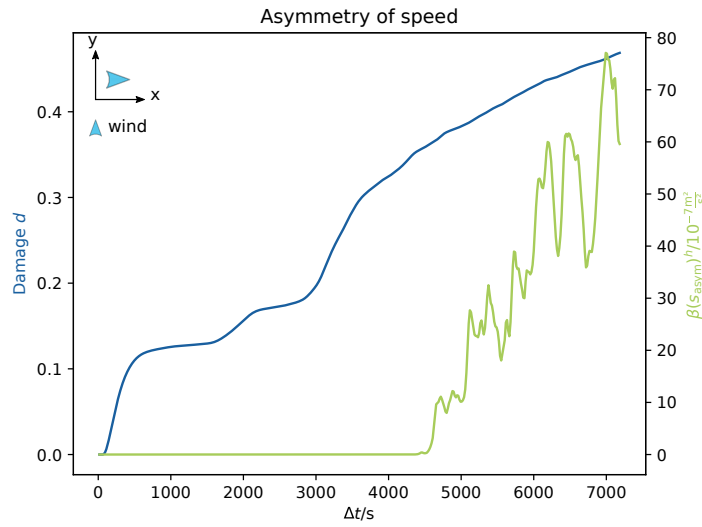
Figure 7.2: Evolution of the asymmetry of speed s_{asym} with the relative variance of asymmetric speed $\beta(s_{\text{asym}})^h$ in green and the domain averaged damage per time step in dark blue for a simulation with external wind forcing in the x-direction.
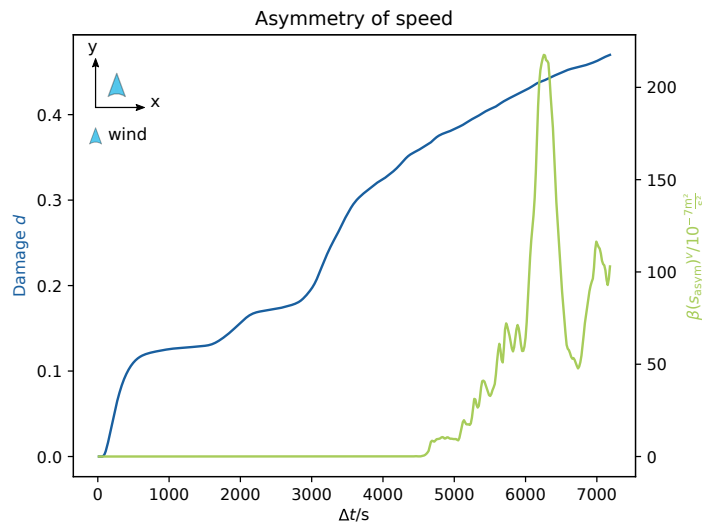
Figure 7.3: Evolution of the asymmetry of speed s_{asym} with the relative variance of asymmetric speed $\beta(s_{\text{asym}})^v$ in green the domain averaged damage per time step in dark blue for a simulation with external wind forcing in the y-direction.
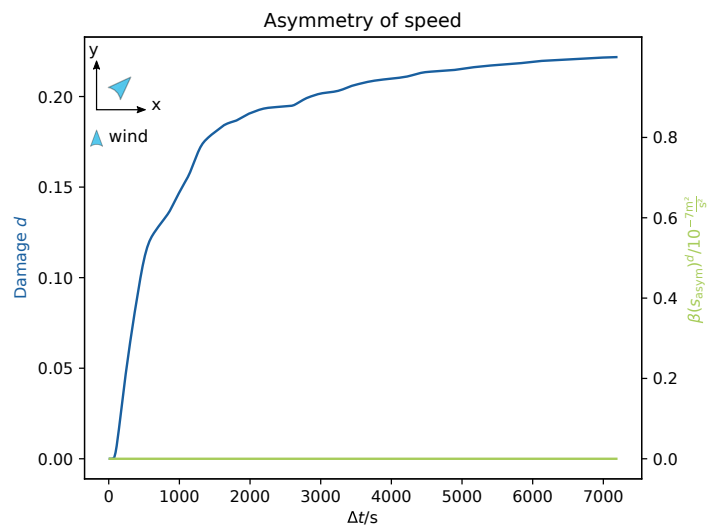
Figure 7.4: Evolution of the asymmetry of speed s_{asym} with the relative variance of asymmetric speed $\beta(s_{\text{asym}})^d$ in green and the domain averaged damage per time step in dark blue for a simulation with external wind forcing along the diagonal in the positive x- and the y-direction.

7.2 Comparing with another MEB Implementation
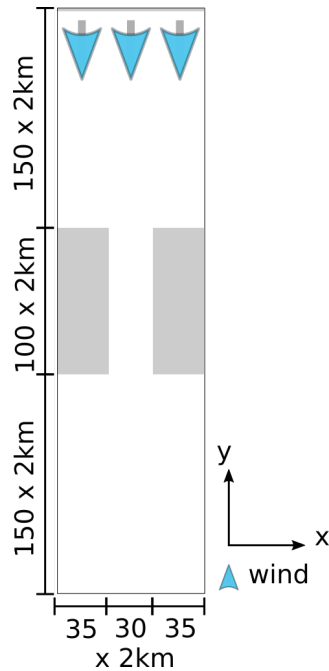
Figure 7.5: Illustration of downstream ice arch.

The second test set-up is a domain that is periodic in the x-direction and features "islands" with a channel in the y-direction (Figure 7.5). The closed ice cover is forced by the wind in a negative y-direction. With this configuration, the results can be directly compared to the MEB model of Plante et al. (2020) and their reference run. The behaviour of ice being advected through a channel is a common test to qualitatively assess the dynamic sea ice pattern through constrictions (cf. Dumont et al. 2009, Dansereau et al. 2017, West et al. 2022).

The MEB implementation used in Plante et al. (2020) is the one of McGill VP sea ice model (Tremblay et al. 1997). McGill's sea ice model is not coupled to an ocean. The numerical framework of Plante et al. (2020) is very similar to the MITgcm in that it uses the finite differences method on a C-grid. The difference between the two frameworks is the treatment of the nonlinear part of the momentum equation, which is solved simultaneously using an IMplicit-EXplicit (IMEX) (Lemieux et al. 2014) approach in Plante et al. (2020)s framework. In the MITgcm the momentum equations are solved implicitly with a Picard solver and only the damage is included via IMEX. Both frameworks use a Flexible General Minimum RESidual method (FGMRES) to solve the linearised momentum equations. In contrast to McGill's framework, the damage is advected in the MITgcm framework.

The channel configuration (Figure 7.5) leads to landfast sea ice. Landfast ice or fast ice is sea ice that forms along and is attached to the coast, for example, between schoals or icebergs (World Meterological Organization 1970).

When such sea ice is driven through a narrow channel, an ice arch can form at the end of the channel and the ice upstream of the arch is locked. Sea ice can exhibit self-obstruction to flow by forming stress-free areas in a curved concave shape. The formation of an ice arch within a narrow channel impedes the flow through the channel (Sodhi 1977).

Sea ice divergence downstream of the channel leads to open water. When an ice arch collapses, the outflow of the channel increases drastically. Therefore, ice arches are an example of large-scale sea ice patterns triggered by small-scale sea ice deformation events leading to long-lasting discontinuities in the ice. Observed and studied ice arches are the Nares Strait and Lincoln Sea ice bridge (Kozo 1991, Dansereau et al. 2017 and Dumont

et al. 2009).

This test aims to recreate Plante et al. (2020) observations and to show that the formation of ice arches is possible with the new implementation within the MITgcm, too. The test experiment is 800 km long and 200 km wide with a grid resolution of 2 km. The channel itself is 200 km long and 60 km wide. The boundary condition at the sides ($x = 0$ km, $x = 200$ km) is periodic, closed in the North and open in the South. External wind forcing increases the surface stress linearly from 0 to 0.625 N/m^2 within 10 h in the simulation. The model parameters can be found in Table 7.1 in the right column.

The overall behaviour of the dynamics is identical to the results shown in Plante et al. (2020). The invariant stress components show the same physical behaviour (see Figure 7.6, Figure 7.7 and Figure 7.8). Plante et al. (2020) uses the opposite sign convention, therefore the negative divergent stress of the MITgcm results is used for the comparison. The stress values are similar at all three different stages of the simulation.

In Figure 7.6, after 300 s ($\tau = 0.005$ N/m^2), both results show large tensile stresses on the downstream coastline, compressive stresses on the upstream coastline and shear stresses in the four corners of the channel. The ice is being pushed into the narrow channel while moving away from the boundaries in the North and the lower boundaries of the channel. Up to this point, no significant damaging events have happend (not shown) as described in Plante et al. (2020). In Figure 7.7, after 3300 s ($\tau = 0.06$ N/m^2), the general appearance of stress fields are similar to the stress field at 300 s ($\tau = 0.005$ N/m^2) only the stress values have increased significantly. A concave shape at the southern end of the channel is visible in both simulations. In Figure 7.8, after 11 700 s ($\tau = 0.2$ N/m^2), divergent and shear stress have formed triangular shapes north of the channel entrance and the area below the channel is stress free. Again the results of the MITgcm align with the results in Plante et al. (2020).

For a more detailed comparison, the evolution of damage over time was analysed and different stages of damage were compared to observe the formation of an ice arch. The results generated with the MITgcm framework can be seen in Figure 7.9 and are compared to the results shown in Figure 7.10. Compared to Plante et al. (2020)'s simulation, the damaging events are less localized in time and happen with smaller forcing. However, the overall dynamic is the same. At the beginning (point I in Figure 7.9), the tensile stresses downstream of the channel increase and a damage line south of each channel boundary appears. With the time, the tensile stresses as well as the shear, stresses in the downstream corners of the channel, increase so that a damage line along the downstream coastline forms (point II in Figure 7.9). This damage line extends over the channel connecting both downstream corners triggered by the further increasing tensile and shear stresses in this area. This is how the ice arch starts to form (Plante et al. 2020). When the ice arch has formed, both divergent and shear stress (left and right panels in Figure 7.7b) exhibit a concave shape at the downstream end of the channel. The divergent stress in the middle of the channel is close to zero. The ice does not experience compressive stresses within the channel. The effect of the ice arch can be seen in the sea ice drift (Figure 7.11).

(a) Divergent stress σ_I (left) and shear stress σ_{II} (right) in the reference simulation Plante et al. (2020).

(b) The negative divergent stress σ_I (left) and the shear stress σ_{II} (right) after a simulation time of 300 s and $\tau = 0.005\,\text{N/m}^2$.
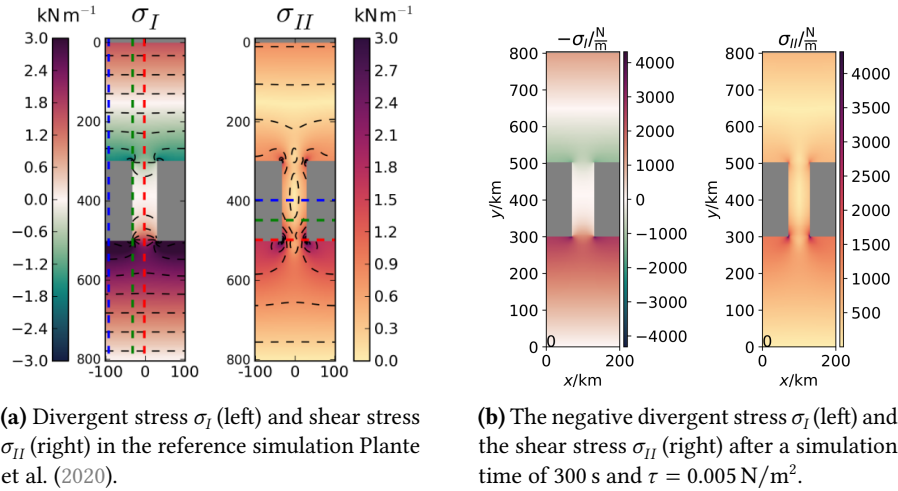
Figure 7.6: Results of downstream ice channel experiment in Plante et al. (2020) (left) and the MITgcm (right) before the formation of an ice arch.

(a) Divergent stress σ_I (left) and shear stress σ_{II} (right) in the reference simulation (Plante et al. 2020).

(b) The negative divergent stress σ_I (left) and the shear stress σ_{II} (right) after a simulation time of 3300 s and $\tau = 0.06\,\text{N/m}^2$.
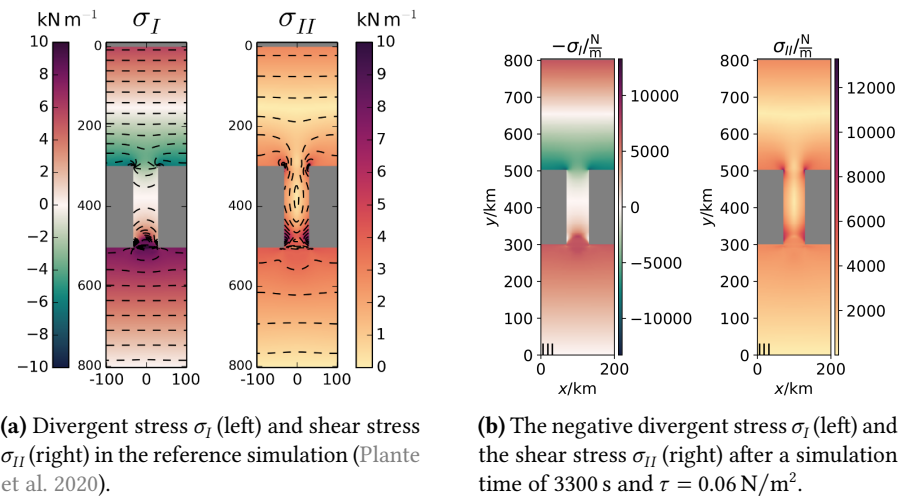
Figure 7.7: Results of downstream ice channel experiment in Plante et al. (2020) (left) and the results of the MITgcm (right) in which the ice arch starts to form.

37

(a) Divergent stress σ_I (left) and shear stress σ_{II} (right) in the reference simulation by Plante et al. (2020).

(b) The negative divergent stress σ_I (left) and the shear stress σ_{II} (right) after a simulation time of 11 700 s and $\tau = 0.2\,\mathrm{N/m^2}$.
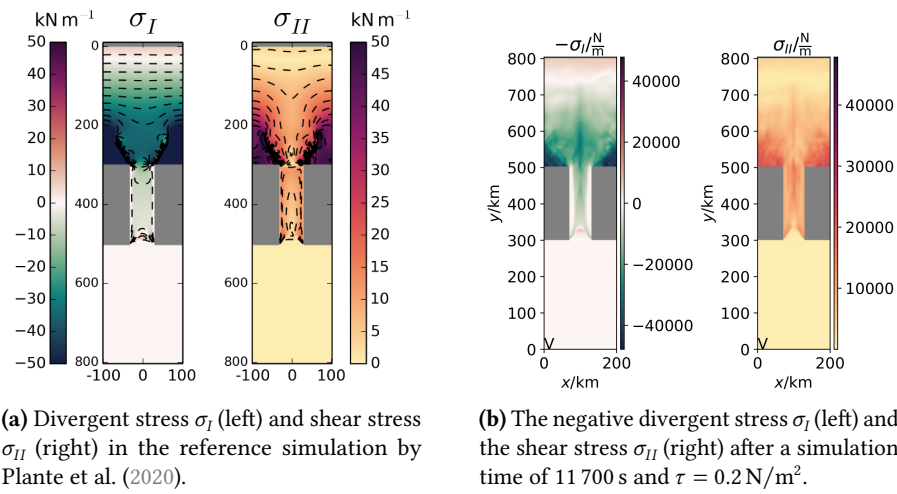
Figure 7.8: Results of downstream ice channel experiment in Plante et al. (2020) (left) and the results of the MITgcm (right) after the ice has detached in the South of the channel.
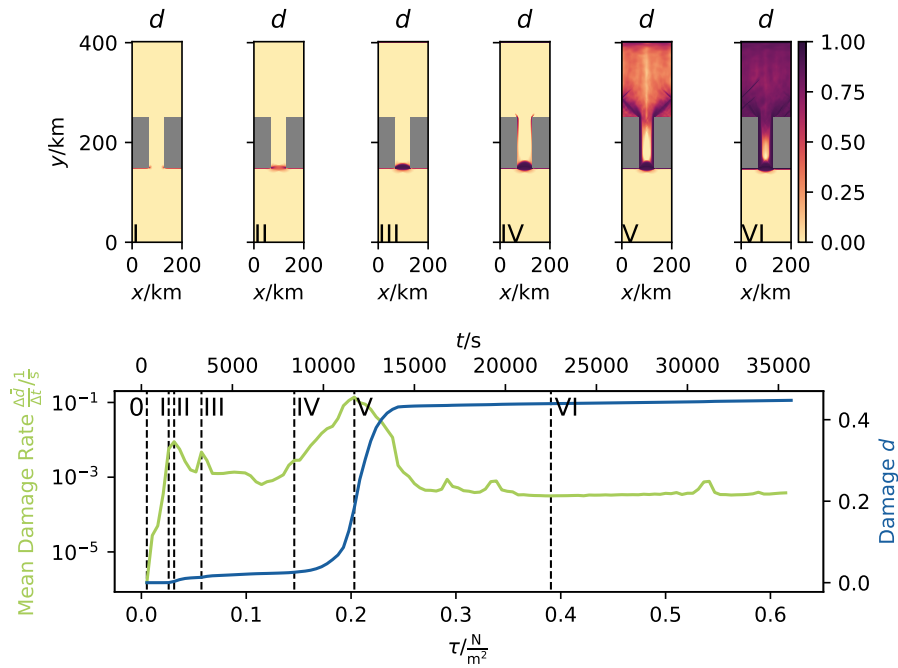
Figure 7.9: Time evolution of the mean domain damage rate (below) and snapshots of damage fields at the with dashed lines indicated times/forcings (above). The dasehd line marked with 0 indicates a time/forcing with negligibly damage.
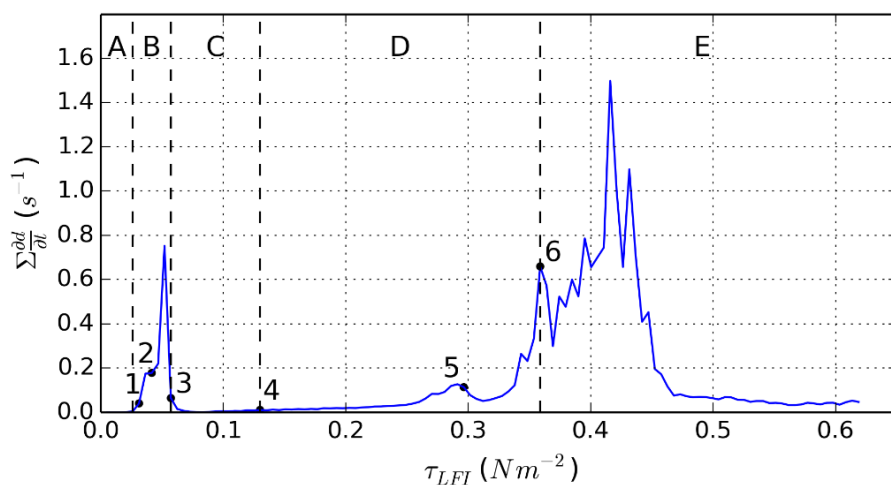
Figure 7.10: Time evolution of the mean domain damage for the McGills framework with dashed lines indicating the beginning and end of simulation phases described by Plante et al. (2020).

Between snapshots I and III (Figure 7.11), the ice bridge builds up. In snapshot III (Figure 7.11), the sea ice has detached from the coastline in the North. In IV (Figure 7.11), the ice at the channel walls is detached and no longer landfast sea ice. The ice north of the channel does not move because it is still one undamaged block of ice. Because the ice north of the channel cannot move yet, tensile forces south of the channel lead to damage and detachment there. The ice mass has split up into a moving part south of the channel and a still resting part north of the channel. Both shear and divergent stress fields south of the ice channel drop to zero when the ice detaches (Figure 7.8b). The ice south of the channel is drifting, accelerated by the wind forcing. What can be observed is not yet due to the formation of the ice bridge. At the time V, damage lines connecting the corners of the channel entrance and the sides north of the channel have been formed (Figure 7.9). The ice north of the channel could be moving without the effect of the ice bridge. Consequently, the same blocked ice in the North can be seen as described in Plante et al. 2020. At the time VI, the ice north of the channel is, after all, strongly damaged and moves (Figure 7.9, Figure 7.11). Plante et al. (2020) speak of a collapse of the ice arch.

The highly damaged ice north of the ice channel is a difference to the reference simulation. After the damage lines along the sides in the North of the domain show up, more and more damage lines appear, also in the middle of the ice field. Also, the damage lines are not symmetric even though the experimental set-up is. Therefore, the asymmetric part of the stresses was analysed. The analysis (not shown) showed that the damage is localized in time until asymmetry kicks in, so there is no systematic error leading to the high increase

in damage. One can also observe periodic elastic waves, which originate in the elastic part of the rheology. After more time has passed, all ice is damaged. Plante et al. (2020) observed highly damaged ice as well and attributed it to a residual error of the solver (see Plante et al. 2021). The same problem likely arises in the MITgcm because of the similarity of the two implementations. Plante et al. (2021) proposed a new damage parameterization that can be tested to be implemented into the MITgcm framework in the future. The damage in the MItgcm is advected in contrast to Plante et al. (2021) and different advection patterns can be observed. The latter can be an explanation to why damage appears in earlier stages and stress increases faster than in the reference run.

As described, the same blocking of ice within the channel was observed with the MITgcm as in Plante et al. (2020), but the effect of the boundary conditions and the ice arching effect itself cannot be distinguished in the test with closed boundaries in the North. The boundary condition at the northern boundary is closed following Plante et al. (2020). To implement this in the test set-up, there is a no-slip condition meaning "no flow" for normal velocities at the boundary. Before the ice can move the inner stress has to overcome the critical values in tension and/or compression. The boundary condition, therefore, has a decelerating effect on the sea ice dynamic. It cannot be said with complete certainty that the ice north of the ice arch does not move at the time V when it is detached from the sides only because of the ice arch. It could still be the deceleration of the boundary condition. To see the effect of the ice arch separately, the ice channel experiment was modified. The modifications follow other ice arch experiments (Dumont et al. 2009, Dansereau et al. 2017 and West et al. 2022). In this experiment, this means opening the boundary in the North, adding walls all along the sides and quadruplicating the simulation time. After 10 h of simulated time with linearly increasing forcing as before, the simulation is run for another 30 h with no further increase of the forcing. In this case, the ice sheet starts to flow as observed before, after being stuck and slows down again. In the second experimental set-up, the ice in the North does not have to detach before it moves and the stopping is caused only by the ice arch. The effect of the ice arch can be seen in the ice drift pattern (Figure 7.12). The velocity north of the channel in the y-direction increases approximately for the first 15 h of the experiment and starts to slow down afterward. The maximum ice velocity at one grid cell north of the channel in a negative y-direction is 0.15 m/s. Within the modeled 40 h the ice does not come to a complete stop, but the evolution of the ice velocity in y-directions indicates a continuous decrease. In a longer run (not shown) even more slowing down of the ice could be seen.

Following Dansereau et al. (2017) in their argumentation for a higher cohesion to see the effect of an ice arch a cohesion of 30×10^3 $1/m^2$ was chosen. Knowing that the formation of an ice arch depends on several other parameters than the cohesion c, in the MITgcm an ice arch was only observed for a cohesion of $c = 30 \times 10^3$ $1/m^2$ and not for cohesions of $c = 10 \times 10^3$ $1/m^2$ or $c = 20 \times 10^3$ $1/m^2$.

Except for the highly damaging events caused by asymmetry the results show that the model can capture stable ice arches in a channel and therefore satisfies the requirement to

model realistically long-lasting and large-scale discontinuities of sea ice.
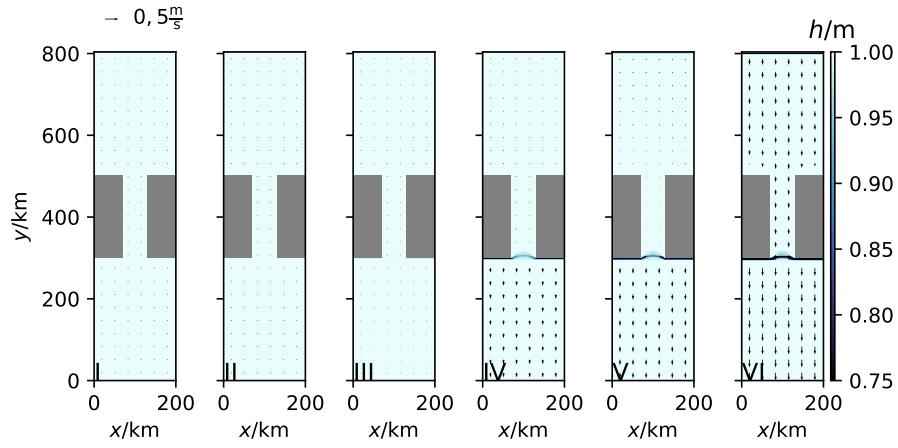
Figure 7.11: Snapshots of the effective ice thickness h and the ice drift velocity (arrows) at the same times (I, II, III, IV, V, VI) as in Figure 7.9.
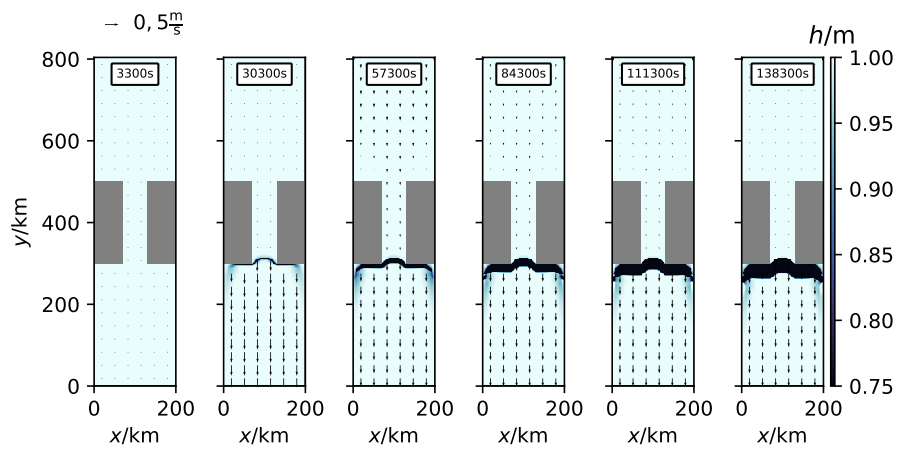
Figure 7.12: Snapshots of the effective ice thickness h and the ice drift velocity (arrows) for an ice channel with open boundaries in the North and the South.

8 Direct Comparison to Results of a Viscous-Plastic Model

In chapter 6 and chapter 7, the framework in which a MEB rheology can be used instead of the VP rheology without changing any of the other model components, was set-up and tested. In this chapter, the framework is used to directly compare LKF formation and sea ice deformation to previous results with a VP rheology by Mehlmann et al. (2021). Afterwards, the reported issues with the VP rheology, which led to the idea of the MEB rheology, in the first place by Girard et al. (2011), are discussed again based on the possibility of using comparable parametrisations of sub-grid variability in the sea ice strength in both VP and MEB rheology.

LKFs are areas where the deformation is highly localized. They can divide the ice cover into different floes that are then akin to solid bodies. Consequently, LKFs greatly influence the sea ice dynamics, the mass balance and the matter exchange between the ocean, ice and atmosphere and it is important to model LKFs correctly.

8.1 Reproduction and Comparison of Sea Ice Dynamics

Mehlmann et al. (2021) introduced a benchmark problem to analyse the capability of different VP models to simulate sea ice deformation, in specific LKFs. The benchmark problem is an idealised quadratic ice field driven by an anticyclonic (clockwise) ocean circulation and moving atmospheric cyclone (see Figure 8.1a). The atmospheric cyclone has a maximum velocity of $30/e$ ms^{-1}, which equals approximately 11 m/s. The cyclones center travels from the center to the upper right corner. The ice field dimensions are (512 x 512) km. To explore the effect of grid resolution on spatial heterogeneity, the grid spacing Δx is varied between 2 km, 4 km and 8 km. The experiment is run for 2 days with a time step $\Delta t = 120$ s. Ocean dynamics and thermodynamic processes are neglected. The initial ice conditions have a constant ice concentration $a = 1.0$ and an initial ice thickness $h^0(x, y)$ of 0.3 m with small perturbations

$$h^0(x, y) = 0.3 \,\mathrm{m} + 0.005 \,\mathrm{m} \left(\sin\left(\frac{60x}{1000 \,\mathrm{km}} \right) + \sin\left(\frac{30y}{1000 \,\mathrm{km}} \right) \right) \tag{8.1}$$

where x, y are given in km. No-slip and "no-flow" boundary conditions are applied on the solid (land) boundaries around the domain. The set of parameters used to run the

(a) Illustration of quadratic ice field driven by an anticyclonic (clockwise) ocean circulation and moving atmospheric cyclon.

(b) Results of the sea ice concentration a with arrows indicating the ice drift velocity after 2 h of simulation of the original benchmark problem by Mehlmann et al. (2021). The data can be found here: https://doi.org/10.17632/kj58y3sdtk.1.
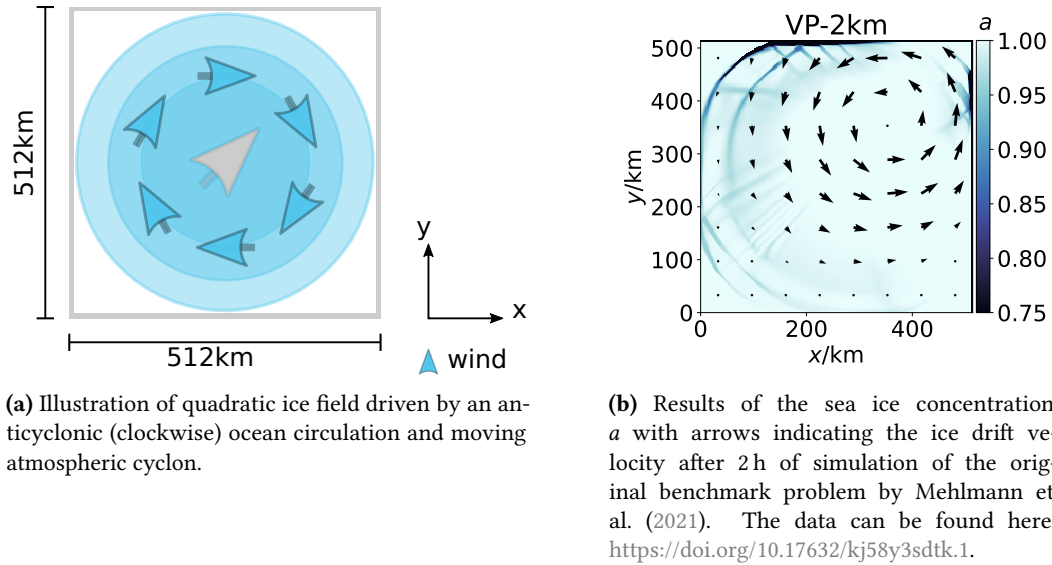
Figure 8.1: Idealized set-up and results of the benchmark problem by Mehlmann et al. (2021).

model can be found in Table 8.1. The simulation using the VP rheology uses the same JFNK solver as in the reference. For more details, see Mehlmann et al. (2021).

In the first step, the solutions of the benchmark problem (Mehlmann et al. 2021) were reproduced with the VP rheology. The reproduced snapshot of the sea ice concentration a after 2 h (Figure 8.2 in the lower left-hand corner) agrees with the results of the original data of the benchmark problem (Mehlmann et al. 2021) shown in Figure 8.1b. Quantitatively, the number of detected LKFs was compared. Mehlmann et al. (2021) found 51 ($\Delta x = 2$ km), 31 ($\Delta x = 4$ km) and 7 ($\Delta x = 8$ km) LKFs. In the reproduced simulation 72 ($\Delta x = 2$ km), 31 ($\Delta x = 4$ km) and 7 ($\Delta x = 8$ km) LKFs were found. Hence, the results with a grid resolution of $\Delta x = 4$ km and $\Delta x = 8$ km were replicable and the results with $\Delta x = 2$ km deviate. As the model configuration and all parameters in both the model and the LKF detection algorithm are identical, the difference in the number of LKFs detected is attributed to truncation errors on different computer platforms. In spite of the apparently large difference in LKFs, the actual difference between the runs are small: the deviation of the mean sea ice concentration of the reproduced 2 km resolution simulation is on the order of 1×10^{-5} (not shown). The tracking algorithm and further discussion of the LKF analysis follows in section 8.2.

In the second step, the same benchmark problem was simulated using the MEB rheology. MEB-specific model parameters can be found in Table 8.1. The damage time T_d is set to the size of a time step Δt. In contrast to the VP simulation, the MEB simulation includes a healing process of the ice, which, however, does not have a big effect on the short time scale

Table 8.1: Model parameters of benchmark problem for the VP rheology and the MEB rheology.

Parameter	Definition	VP	MEB	Unit
T_d	Damage time		120	s
T_h	Healing time		1×10^5	s
E_0	Elastic modulus		5×10^8	N/m
P^*	Ice strength	27.5×10^3		N/m
ν	Poisson ratio		0.3	
λ_0	Viscous relaxation		1×10^7	N s/m
μ	Internal friction		0.7	
c_0	Cohesion		25×10^3	N/m
e	Ellipse aspect ratio	2		
ρ_a	Air density	1.3	1.3	$1/\text{m}^3$
ρ_i	Sea ice density	9×10^2	9×10^2	$1/\text{m}^3$
ρ_w	Water density	1.026×10^3	1.026×10^3	$1/\text{m}^3$
C_a	Air drag coefficient	1.2×10^{-3}	1.2×10^{-3}	
C_w	Water drag coefficient	5.5×10^{-3}	5.5×10^{-3}	
f_0	Coriolis parameter	1.46×10^{-4}	1.46×10^{-4}	$1/\text{s}$
C^*	Ice concentration parameter	20	20	

of the simulation. The parameter for the Elastic modulus is set to $E_0 = 5 \times 10^8\,\text{N/m}$ and the cohesion is set to $c_0 = 25 \times 10^3\,\text{N/m}$. Those are the same values as in chapter 7. Again, the solver is the Krylov solver with an implicit-explicit method used for the damage as in section 7.2. To compare the ice dynamic, snapshots of the ice drift and ice concentration (Figure 8.2) and the principle stresses (Figure 8.3, Figure 8.4) after 2 h of simulated time are shown.

The ice drift and sea ice concentration show similar behaviour on all spatial resolutions (Figure 8.2). Higher ice drift velocities can be observed with the VP model. Also, the simulated sea ice concentration *a* with the VP rheology shows more details than the MEB rheology. Darker blue lines marking low ice concentration show a different pattern. While the MEB rheology has mostly circular features, the VP simulation also has radial features. The same features are visible in the principal stresses (Figure 8.3, Figure 8.4). The divergent stress (Figure 8.3) shows one of the main differences in both used rheologies. While the MEB rheology allows tensile stresses, the VP rheology with the commonly used elliptical yield curve does not. Also, stress values of the MEB rheology are twice the size of the

VP values. It is difficult to directly compare values for the stress because they depend on different yield curves (cf. Figure 4.2). For high values on the σ_I-axis, the MEB yield curve allows substantially higher values on the σ_{II}-axis. Comparing the σ_{II}-values inside the MC-yield curve at the width of the ellipse to the highest σ_{II}-values of the ellipse, a factor 2 in between these is possible. Depending on the sea ice strength P^* and the parameters defining the MC-yield curve, even higher differences between the allowed σ_{II}-values are possible. The shear stress snapshots in Figure 8.4 and the divergent stress snapshots in Figure 8.3 for the MEB rheology show that the MEB rheology also produces gradients in the ice.

It was shown that a direct comparison between the VP and the MEB rheology is possible with the MITgcm. Furthermore, the results of the model using the MEB rheology are reassuring concerning the capability of the MEB model to simulate sea ice deformation in a more complex set-up with an ocean circulation and an atmosphere cyclone as forcing.
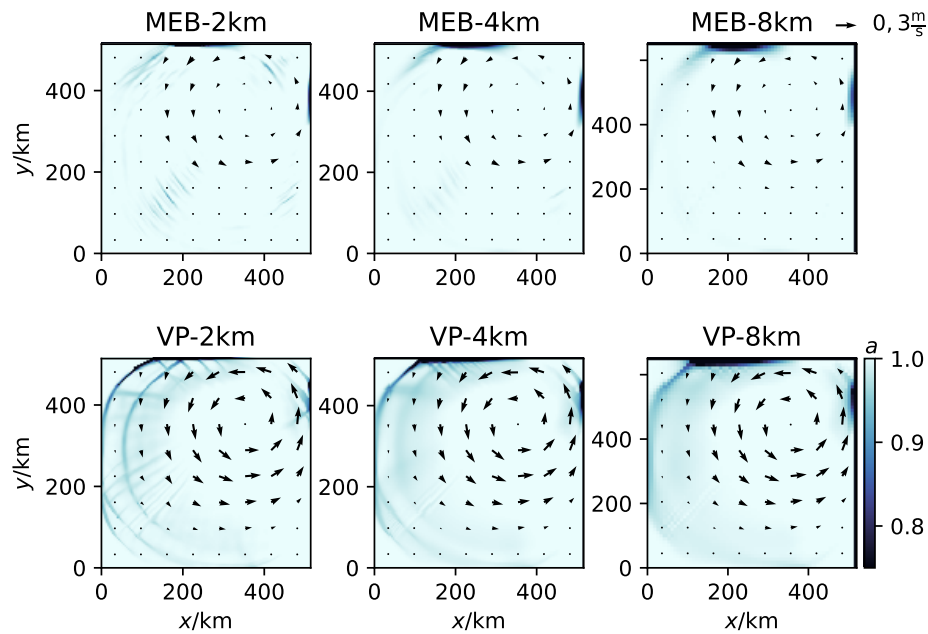
Figure 8.2: Snapshot of the ice concentration a with arrows indicating the ice drift velocity after 2 h in the simulation. Results for simulations using the VP rheology below and for simulations using the MEB rheology above.
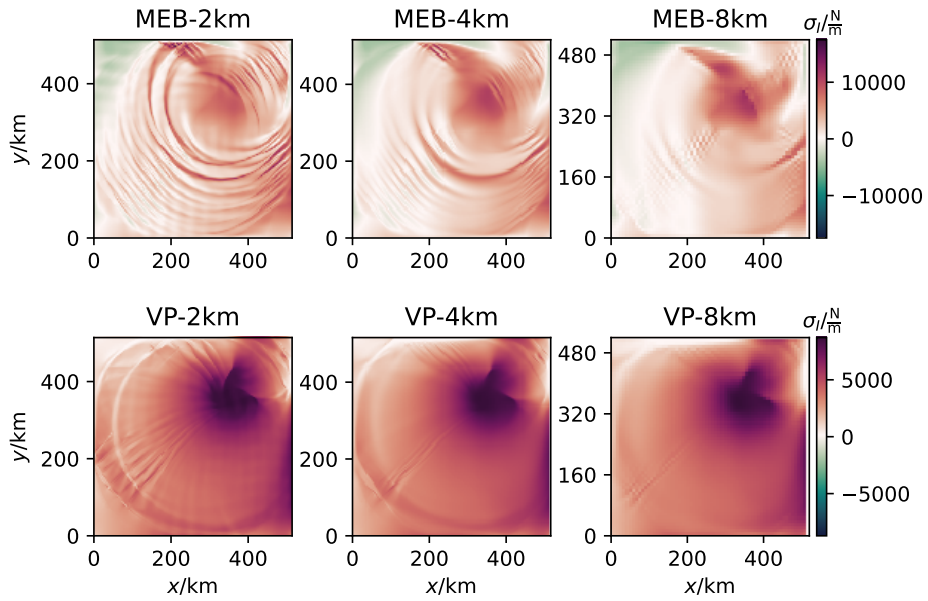
Figure 8.3: Snapshot of the divergent stress field σ_I of the MEB simulation above and the VP rheology below. The snapshots are taken after 2 h in the simulation.
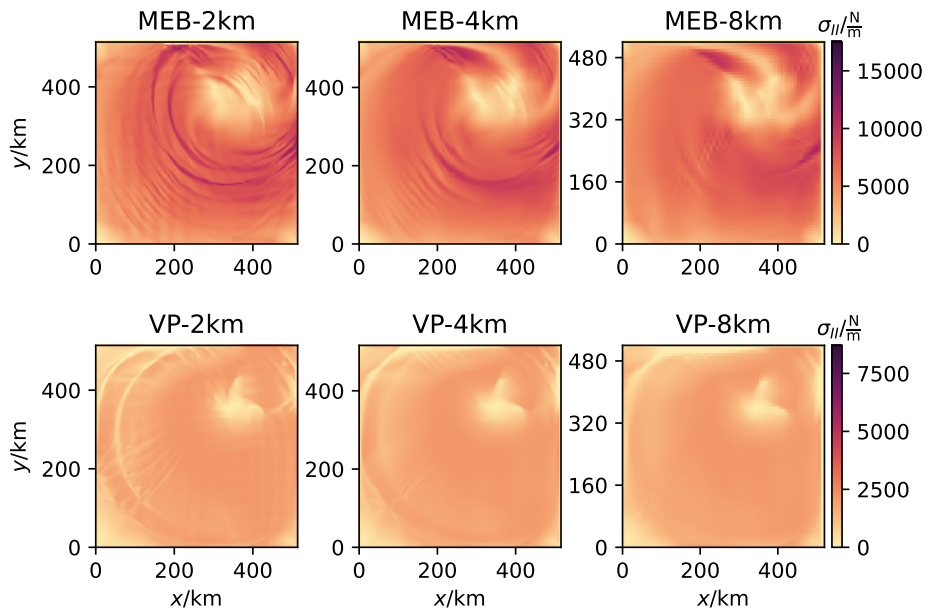
Figure 8.4: Snapshot of the shear stress field σ_{II} of the MEB simulation above and the VP rheology below. The snapshots are taken after 2 h in the simulation.

8.2 Linear Kinematic Features

The analysis of the number of LKFs is used to compare the results of Mehlmann et al. (2021) to the reproduced results in more detail. The tracking algorithm of Hutter et al. (2020) was used for identifying the LKFs. LKFs are characterized by large gradients in the deformation field and therefore can be tracked by classifying higher deformation rates compared to surrounding ones. The tracking algorithm consists of three steps: the preprocessing of the data to create a binary map of pixels, splitting the high-deformation pixels into the smallest possible segments and reconnecting the segments depending on their distance and orientation relative to each other.

The tracking algorithm by Hutter et al. (2020) is applied with some modifications following Mehlmann et al. (2021) to the shear deformation rate $\dot{\varepsilon}_{II}$ (4.12). To preprocess the data and detect LKF features, the local differences in the field across different scales are emphasized by using the natural logarithm of the field. Then a difference of Gaussian filter, acting as a bandpass filter, is used to pick the highest differences in this field. The parameters of the bandpass filter define the range of LKFs by setting a lower and an upper limit. The output is a list of pixels belonging to LKFs. In the last step the algorithm identifies the pixels that belong to the same LKF by making statistical assumptions based on the pixel's distance, difference in orientation and difference in the shear deformation rate. The complete tracking algorithm can be found in Hutter et al. (2020). The parameters to tune the algorithm are the same as Mehlmann et al. (2021) used. An example of tracked LKFs in the shear deformation field is given in Figure 8.5b.

Following Mehlmann et al. (2021), a larger number of LKFs for a wider grid spacing is one attribute for a good capability to simulate sea ice dynamics. Mehlmann et al. (2021) considered three attributes: the number of LKFs, the length of LKFs and the direct visual evaluation of the approximation. More refined LKFs were found as the spatial resolution increases. Mehlmann et al. (2021) associated the formation of LKFs with the staggering and discretization of the velocity vector components on the grid with a given spatial resolution. In the used set-up, the staggering of the velocity vector components is the same for both rheologies.

The number of detected LKFs depending on the grid space Δx for the VP and MEB simulation can be found in Figure 8.5a marked with crosses. The numbers in both cases increase with increasing resolution. But, the number of LKFs for the VP rheology increases more than the numbers of LKFs of the MEB simulations. More LKFs were generally detected with the VP rheology for $\Delta x = 2$ km and $\Delta x = 4$ km. For a resolution of $\Delta x = 8$ km, the same number of LKFs was found. The results show that the MEB rheology is able to model LKFs.

Furthermore, the stress snapshots (see Figure 8.3 and Figure 8.4) show more spatial heterogeneity for the simulations using the MEB rheology consistent with Girard et al. (2011) at first sight. But the spatial heterogeneity measured by the number of LKFs does not

confirm this because it is higher for the simulation with the VP rheology than with the MEB rheology. Therefore, further analysis of spatial heterogeneity follows in section 8.3.
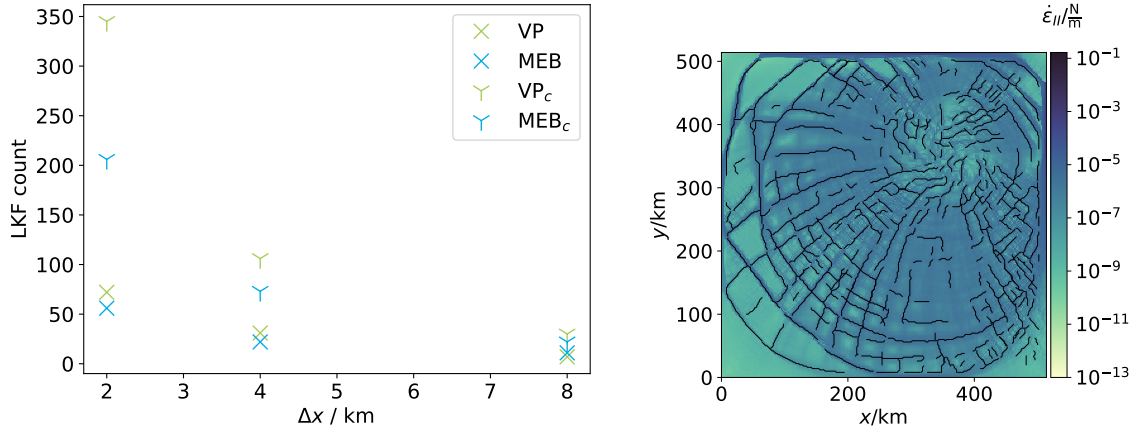
(a) Number of LKFs for both VP and MEB rheology for simulations with 2 km, 4 km and 8 km grid spacing Δx. The index "c" indicates that the simulations used a stochastically perturbed ice strength.

(b) The shear deformation rate $\dot{\varepsilon}_{II}$ in a 2 km simualtion with VP rheology using a stochastically perturbed ice strength P^*. The tracked LKFs are plottet in black.

Figure 8.5: LKF analysis for direct comparison of VP and MEB and to show spatial heterogeneity in both rheologies.

8.3 Spatial Heterogeneity

Motivated by the observations of section 8.2 that the number LKFs is not necessarily larger for models using the MEB rheology as predicted, the set-up is used to investigate another way to create spatial heterogeneity.

Girard et al. (2011) and Dansereau et al. (2017) used a variable cohesion parameter c instead of a constant cohesion. In both references, the cohesion parameter c was randomly drawn from a uniform distribution to account for faults and cracks in the ice below the spatial grid scale Δx. The same was done within the MITgcm framework for the MEB rheology. The cohesion c_0 at each grid cell was multiplied by a value drawn between 0.5 and 1.5. This led to a heterogeneous cohesion field throughout the simulation. Along with the cohesion, the yield curve of the MEB rheology changes (cf. Equation 4.24) because the critical uniaxial compressive stress σ_c changes. Consequently, a noisy cohesion leads to a different damage criterion for each grid cell. The damage criterion in a grid cell does not vary with time.

The benchmark problem was repeated with the modified cohesion and the results show a significant increase in the number of LKFs for each grid resolution (see Figure 8.5a blue y-shaped crossses). The number of LKFs for the MEB simulation with noisy cohesion is higher than for the VP simulation. With this modification the results confirm the statement of Girard et al. 2011. The shear deformation rate snapshot in Figure 8.6, shows similar results to Girard et al. (2011) and Dansereau et al. (2017) concerning spatial heterogeneity. Also, the shear deformation rate for the lowest grid resolution (Δx =8 km) shows remarkable spatial heterogeneity compared to the shear deformation rate without the use of stochastically perturbed parameters for the cohesion or the ice strength (Figure 8.7).

Nevertheless, a second test was made in which a comparable variability within the ice was added to the VP rheology. The idea is to give the VP simulation the same material heterogeneity and to use the framework in which VP and MEB rheology can be directly compared.

As there is no explicit cohesion parameter in the VP model, the ice strength parameter P^* was multiplied with the same random field drawn from a uniform distribution as the cohesion in the MEB rheology. The ice strength parameter P^* also changes the yield curve and increases or decreases the cohesive properties of the ice as described in section 4.4. In contrast to the MEB rheology, the VP yield curve can further change throughout the simulation because of the dependency of the maximum compressive stress P of the ice thickness h and the ice concentration a (cf. Equation 4.18).

The number of LKFs of the modified VP simulation are even higher than the results of the modified MEB simulation (Figure 8.5a green y-shaped crosses). Also, the difference between the VP rheology with and without a noisy ice strength parameter P^* is bigger than the same difference between the two simulations using the MEB rheology. In comparison, the number of LKFs in Figure 8.5a for the simulations with variability in the ice strength (green y-shaped crosses) show the same relation as with a constant ice strength (green crosses). The number of LKFs increase with the increase of spatial resolution and the increase is higher for the VP rheology than for the MEB rheology. The shear deformation field with the detected LKFs for the benchmark experiment after 2 h with $\Delta x = 2$ km with a perturbed ice strength is shown in Figure 8.5b.

These results (Figure 8.5a) do not support the statement that VP cannot have the same spatial heterogeneity as the MEB rheology (Girard et al. 2011). Note, that here the random ice strength perturbabtion was similar in both rheologies, whereas Girard et al. (2011) compared a VP model with smooth ice strength to an EB model with randomly perturbed cohesion. The results suggest that ice models with VP rheology reproduce the observed spatial heterogeneity, if the variability within the ice's mechanical properties is stochastically perturbed as the cohesion in the MEB model. The large number of LKFs with the stochastic perturbation of the VP ice strength, compared to the stochastic perturbation of the MEB cohesion, can be explained by the additional intrinsic feedback of the ice state (thickness h, ice concentration a) on the maximal compressive stress P.

It is unclear whether the issues of the VP rheology with the missing spatial heterogene-

ity (Girard et al. 2011) is caused by the rheology itself, or because of missing material heterogeneity such as faults and cracks in the ice below the spatial grid scale. In both rheologies, spatial heterogeneity of the results can be increased by introducing spatial variability within mechanical ice properties.
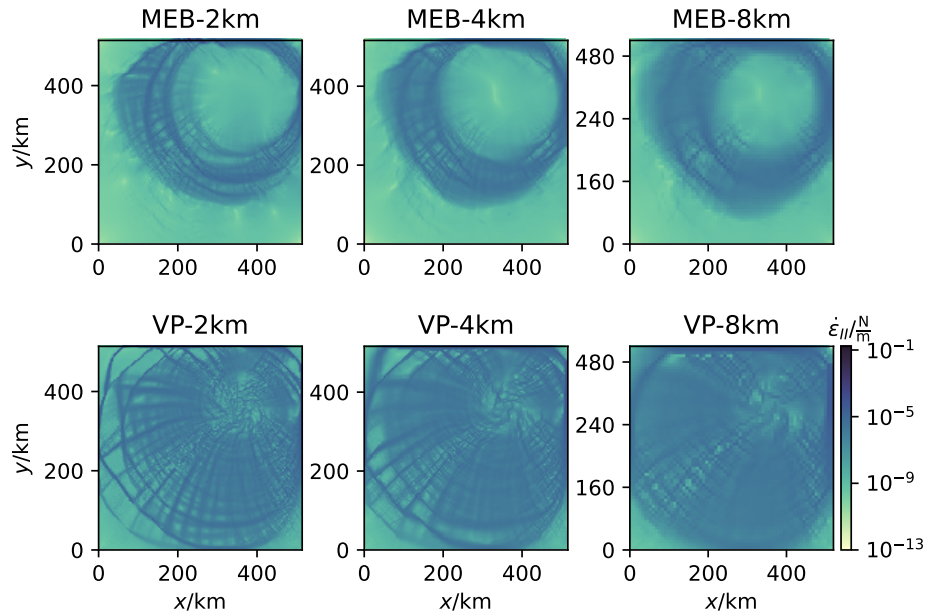
Figure 8.6: Snapshot of the shear deformation rate $\dot{\varepsilon}_{II}$ of the MEB simulation above and the VP rheology below. Both simulations use a stochastically perturbed parameter for the cohesion or the ice strength. The snapshots are taken after 2 h of simulation.
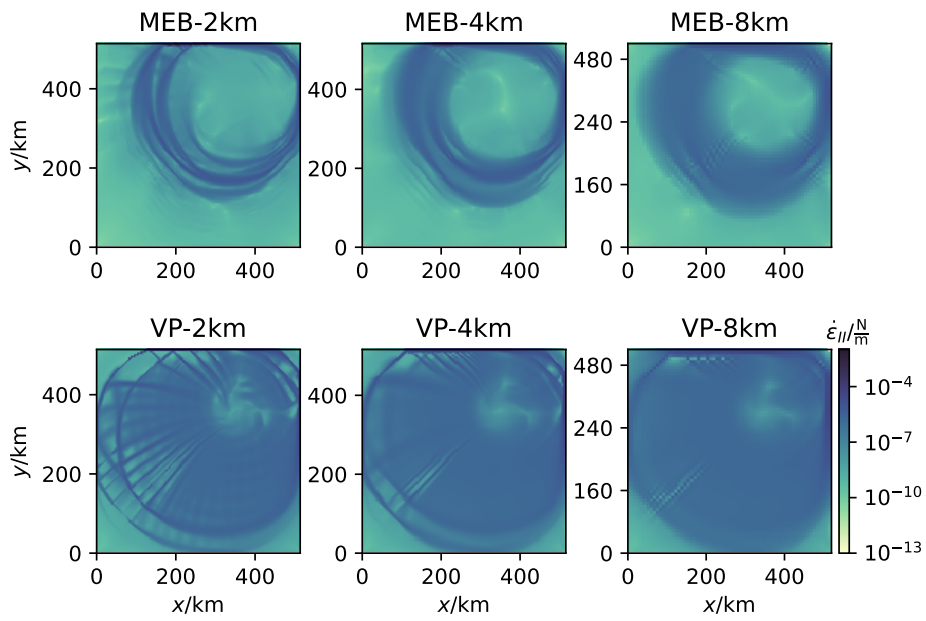
Figure 8.7: Snapshot of the shear deformation rate $\dot{\varepsilon}_{II}$ of the MEB simulation above and the VP rheology below. Without the use of stochastically perturbed parameters for the cohesion or the ice strength. The snapshots are taken after 2 h of simulation.

9 Discussion and Conclusion

In this thesis, an implementation of a MEB rheology in a sea ice model coupled to an ocean model was presented and tested. The main difficulty was to achieve numerical stability. The presented implementation showed the least numerical instabilities when the number of averaging operations was reduced and when three parameters were defined at two grid points (chapter 5). Nevertheless, it is possible to find an even more stable way of treating the variables, especially the damage parametrisation, which can be further improved concerning numerical stability. The tests of the implementation and the comparison with another MEB implementation (Plante et al. 2020) yield confidence in the new implementation, but showed numerical instabilities whenever the simulations developed significant damage in the ice.

The model nearly exactly reproduced simple analytic predictions of an idealized experimental set-up in steady state (chapter 6). In particular, the comparison showed that the averaging between variables of stress does not trigger noise, which supports the double-defined set of parameters. The parametrisation of the damage was not tested with this comparison because the damaging mechanism was turned off to allow the model to reach a steady state.

Idealized, symmetric experiments (section 7.1) showed negligible asymmetry at the beginning of each simulation. This observation also reduces the probability of a significant error in the main part of the implementation. However, the symmetry experiments showed increasing asymmetry with increasing damaging events and small differences between the tests with wind in the x-direction and with wind in the y-direction were found. Both observations can be attributed to a small remaining numerical instability caused by the damage parametrisation. The experiment with wind forcing along the diagonal of the experiment showed no asymmetry. The absence of asymmetry while damage remained low supports the hypothesis that the parametrisation of damage is the reason for the remaining numerical instabilities.

The comparison with Plante et al. (2020) (section 7.2) leads to the same conclusion. On the one hand, the same dynamics of the ice within the channel and the same blocking effect of the ice as in Plante et al. (2020) could be observed which enforces the confidence in the implementation. On the other hand, the highly damaged ice north of the channel and the less localized damaging events in time support the concluded weakness of the damage parametrisation.

Plante et al. (2020) stated to capture the ice arching effect with his model. The results with the MITgcm showed the same arching behaviour as Plante et al. (2020): the ice did not

stop after it had moved, but it did not start to move in the first place. In other similar models (Dumont et al. 2009, Dansereau et al. 2017 and West et al. 2022), the ice flowed through the channel before being stopped by the ice arching effect. In the modified ice channel experiment with the MITgcm, these results could be reproduced: the ice started to move and was stopped afterwards. The second test makes it possible to distinguish between the effect of the boundary conditions preventing the ice from starting to move and the ice being stopped because of the ice arching effect. This test showed with more certainty that the MITgcm ice model can capture the ice arching effect.

With the new MEB implementation, the MITgcm code can now be used as a framework where different rheologies can be compared without confounders. The main features of the ice model are treated in the same way such as the staggering of the velocity fields. Therefore, the framework allows to isolate the effect of the rheologies. The benchmark problem introduced by Mehlmann et al. (2021) was used to directly compare the MEB rheology to the VP rheology (chapter 8). One of the main motivations to develop a brittle rheology was the observation that models with VP rheology underestimate observed spatial heterogeneity (Girard et al. 2011). At first sight, the stress snapshots showed more spatial heterogeneity for the simulations using the MEB rheology, consistent with Girard et al. (2011), but the spatial heterogeneity measured by the number of LKFs did not support the visual impression.

Dansereau et al. (2017) and Girard et al. (2011) used a spatially perturbed cohesion parameter in their MEB and EB rheology, respectively, in contrast to the implementation of the MEB rheology in the MITgcm which follows Plante et al. (2020). Only with this modification, which is a built-in variability at the grid scale, the MEB implementation in the MITgcm reproduces the high spatial heterogeneity reported by Dansereau et al. (2017) and Girard et al. (2011).

The method to increase spatial heterogeneity to a model was applied to simulations using the VP rheology, as well. The results of simulations using the VP rheology with a perturbed ice strength parameter in section 8.3 do not support the statement that VP cannot have the same spatial heterogeneity as the MEB rheology (Girard et al. 2011).

In the results of the direct comparison of the VP and MEB rheology, the heterogeneity of the model depends very much on applying randomly perturbed cohesion or ice strength parameters. The differences between rheologies are much smaller than differences between models with and without perturbed parameters. Girard et al. (2011) based their conclusion on a comparison of VP model with constant ice strength parameter to an EB model with a randomly perturbed cohesion parameter. With this choice, the stronger heterogeneity is built into the model and the comparison appears biased. One can only assume that all subsequent implementations of brittle rheologies contain this build-in randomness, although is it only mentioned explicitly in Dansereau et al. (2016) and Girard et al. (2011).

10 Outlook

The framework of this thesis provides the opportunity for further investigation of the specific effects that different parts of rheologies have on sea ice dynamics. After considering the results of this thesis, some modifications of the MEB and the VP rheology appear useful to further improve the models.

The presented numerical instabilities within the damage parametrisation of the MEB rheology can be further analysed. A possible improvement of the implementation was already suggested by Plante et al. (2021). Above this, an analysis of the energy balance for the stress update in dependency of the damage may be helpful for finding a more numerically stable damage parametrisation.

Additionally, the MEB rheology is missing a healing mechanism coupled to the thermodynamics of the model and an advection scheme for the stresses. For example, the Lagrangian sea ice model by Rampal et al. (2016) introduced a healing mechanism which includes the formation of new ice in open water and a thermodynamical healing driven by the local temperature gradient between the bottom of the ice and the snow-ice interface. In their model, the damage decreases with the formation of new ice and the healing increases with cooler temperatures (Rampal et al. 2016). Another possible improvement for the MEB rheology can be a cohesion coupled to the ice state, such as the sea ice thickness and concentration, comparable to the VP rheology.

Despite the possible improvements of the implementation, the MITgcm framework, as it is, can be already used to compare rheologies. Especially, the discrepancy between the spatial heterogeneity observed for the VP and MEB rheology in this thesis with the former observed problems with the missing spatial heterogeneity of the VP rheology (Girard et al. 2009) needs to be further analysed. Concerning the spatial heterogeneity, the presented results are based only on the number of LKFs. A scaling analysis (Hutter et al. 2018, Girard et al. 2009, Olason et al. 2022) could be used to support or reject the findings. Moreover, further research is needed on the extend to which the spatial heterogeneity depends on the rheology itself, or on the choice of parameters such as the ice strength or cohesion parameter. The MITgcm framework can be used to investigate the effect of introducing spatial variability within mechanical ice properties on the spatial heterogeneity in both rheologies, for example, by setting all parameters constant except one which is perturbed. The same analysis can be made for different ways of perturb-parameter approaches on small scales or stochastic parameter perturbations following Juricke et al. (2013).

Bibliography

Adcroft, A., Hill, C., Campin, J.-M., Marshall, J., and Heimbach, P. (2004). "Overview of the formulation and numerics of the MIT GCM". In: *Proceedings of the ECMWF seminar series on Numerical Methods, Recent developments in numerical methods for atmosphere and ocean modelling*, pp. 139–149.

Campbell, W. J. (1965). "The wind-driven circulation of ice and water in a polar ocean". In: *Journal of Geophysical Research* 70.14, pp. 3279–3301.

Carrieres, T., Buehner, M., Lemieux, J.-F., and Pedersen, L. T. (2017). *Sea ice analysis and forecasting: Towards an increased reliance on automated prediction systems*. Cambridge University Press.

Coon, M., Kwok, R., Levy, G., Pruis, M., Schreyer, H., and Sulsky, D. (2007). "Arctic Ice Dynamics Joint Experiment (AIDJEX) assumptions revisited and found inadequate". In: *Journal of Geophysical Research: Oceans* 112.C11.

Coon, M., Maykut, R., Pritchard, R., Rothrock, D., and Thorndike, A. (1974a). "Modeling the pack ice as an elastic-plastic material". In: *AIDJEX Bull.* 24, pp. 1–105.

Coon, M. and Pritchard, R. (1974b). "Application of an elastic-plastic model of arctic pack ice". In: *Coast and Shelf of the Beaufort Sea*, pp. 173–193.

Cromer, A. (1981). "Stable solutions using the Euler approximation". In: *American Journal of Physics* 49.5, pp. 455–459.

Dansereau, V., Weiss, J., Saramito, P., and Lattes, P. (2016). "A Maxwell elasto-brittle rheology for sea ice modelling". In: *The Cryosphere* 10.3, pp. 1339–1359.

Dansereau, V., Weiss, J., Saramito, P., Lattes, P., and Coche, E. (2017). "Ice bridges and ridges in the Maxwell-EB sea ice rheology". In: *The Cryosphere* 11.5, pp. 2033–2058.

Dumont, D., Gratton, Y., and Arbetter, T. E. (2009). "Modeling the dynamics of the North Water polynya ice bridge". In: *Journal of Physical Oceanography* 39.6, pp. 1448–1461.

Erlingsson, B. (1988). "Two-dimensional deformation patterns in sea ice". In: *Journal of Glaciology* 34.118, pp. 301–308.

Girard, L., Bouillon, S., Weiss, J., Amitrano, D., Fichefet, T., and Legat, V. (2011). "A new modeling framework for sea-ice mechanics based on elasto-brittle rheology". In: *Annals of Glaciology* 52.57, pp. 123–132.

Girard, L., Weiss, J., Molines, J.-M., Barnier, B., and Bouillon, S. (2009). "Evaluation of high-resolution sea ice models on the basis of statistical and scaling properties of Arctic sea ice drift and deformation". In: *Journal of Geophysical Research: Oceans* 114.C8.

Hibler, W. (1974). "Differential sea-ice drift. II. Comparison of mesoscale strain measurements to linear drift theroy predictions". In: *Journal of Glaciology* 13.69, pp. 457–471.

Hibler, W. (1977). "A viscous sea ice law as a stochastic average of plasticity". In: *Journal of Geophysical Research* 82.27, pp. 3932–3938.

– (1979). "A dynamic thermodynamic sea ice model". In: *Journal of physical oceanography* 9.4, pp. 815–846.

Hibler, W. and Schulson, E. M. (2000). "On modeling the anisotropic failure and flow of flawed sea ice". In: *Journal of Geophysical Research: Oceans* 105.C7, pp. 17105–17120.

Hunke, E. C., Lipscomb, W. H., and Turner, A. K. (2010). "Sea-ice models for climate study: retrospective and new directions". In: *Journal of Glaciology* 56.200, pp. 1162–1172.

Hutter, N., Bouchat, A., Dupont, F., Dukhovskoy, D., Koldunov, N., Lee, Y. J., Lemieux, J.-F., Lique, C., Losch, M., Maslowski, W., et al. (2022). "Sea Ice Rheology Experiment (SIREx): 2. Evaluating Linear Kinematic Features in High-Resolution Sea Ice Simulations". In: *Journal of Geophysical Research: Oceans* 127.4, e2021JC017666.

Hutter, N. and Losch, M. (2020). "Feature-based comparison of sea ice deformation in lead-permitting sea ice simulations". In: *The Cryosphere* 14.1, pp. 93–113.

Hutter, N., Losch, M., and Menemenlis, D. (2018). "Scaling properties of arctic sea ice deformation in a high-resolution viscous-plastic sea ice model and in satellite observations". In: *Journal of Geophysical Research: Oceans* 123.1, pp. 672–687.

Ip, C. F. (1993). *Numerical investigation of different rheologies on sea-ice dynamics.* Dartmouth College.

Juricke, S., Lemke, P., Timmermann, R., and Rackow, T. (2013). "Effects of stochastic ice strength perturbation on Arctic finite element sea ice modeling". In: *Journal of climate* 26.11, pp. 3785–3802.

Kozo, T. L. (1991). "The hybrid polynya at the northern end of Nares Strait". In: *Geophysical Research Letters* 18.11, pp. 2059–2062.

Landau, L. and Lifschitz, E. (1989). *Lehrbuch der Theoretischen Physik, Band VII: Elastizitätstheorie.* Akademie-Verlag Berlin.

Lemieux, J.-F., Knoll, D. A., Losch, M., and Girard, C. (2014). "A second-order accurate in time IMplicit–EXplicit (IMEX) integration scheme for sea ice dynamics". In: *Journal of Computational Physics* 263, pp. 375–392.

Lemieux, J.-F., Tremblay, L. B., Thomas, S., Sedláček, J., and Mysak, L. A. (2008). "Using the preconditioned Generalized Minimum RESidual (GMRES) method to solve the sea-ice momentum equation". In: *Journal of Geophysical Research: Oceans* 113.C10.

Losch, M., Fuchs, A., Lemieux, J.-F., and Vanselow, A. (2014). "A parallel Jacobian-free Newton–Krylov solver for a coupled sea ice-ocean model". In: *Journal of Computational Physics* 257, pp. 901–911.

Losch, M., Menemenlis, D., Campin, J.-M., Heimbach, P., and Hill, C. (2010). "On the formulation of sea-ice models. Part 1: Effects of different solver implementations and parameterizations". In: *Ocean Modelling* 33.1-2, pp. 129–144.

Malvern, L. E. (1969). *Introduction to the Mechanics of a Continuous Medium.* Monograph.

Maykut, G. and Untersteiner, N. (1971). "Some results from a time-dependent thermodynamic model of sea ice". In: *Journal of Geophysical Research* 76.6, pp. 1550–1575.

Mehlmann, C., Danilov, S., Losch, M., Lemieux, J.-F., Hutter, N., Richter, T., Blain, P., Hunke, E., and Korn, P. (2021). "Simulating Linear Kinematic Features in Viscous-Plastic Sea Ice Models on Quadrilateral and Triangular Grids With Different Variable Staggering". In: *Journal of Advances in Modeling Earth Systems* 13.11, e2021MS002523.

MITgcm Group (2021). *MITgcm User Manual.* Online documentation. `https://mitgcm.readthedocs.io/en/latest`. Cambridge, MA 02139, USA: MIT. DOI: `10.5281/zenodo.1409237`.

Olason, E., Boutin, G., Korosov, A., Rampal, P., Williams, T., Kimmritz, M., Dansereau, V., and Samaké, A. (2022). "A New Brittle Rheology and Numerical Framework for Large-Scale Sea-Ice Models". In: *Journal of Advances in Modeling Earth Systems* 14.8, e2021MS002685.

Plante, M. and Tremblay, L. B. (2021). "A generalized stress correction scheme for the Maxwell elasto-brittle rheology: impact on the fracture angles and deformations". In: *The Cryosphere* 15.12, pp. 5623–5638.

Plante, M., Tremblay, L. B., Losch, M., and Lemieux, J.-F. (2020). "Landfast sea ice material properties derived from ice bridge simulations using the Maxwell elasto-brittle rheology". In: *The Cryosphere* 14.6, pp. 2137–2157.

Rampal, P., Bouillon, S., Ólason, E., and Morlighem, M. (2016). "neXtSIM: a new Lagrangian sea ice model". In: *The Cryosphere* 10.3, pp. 1055–1073.

Ringeisen, D., Losch, M., Tremblay, L. B., and Hutter, N. (2019). "Simulating intersection angles between conjugate faults in sea ice with different viscous–plastic rheologies". In: *The Cryosphere* 13.4, pp. 1167–1186.

Schulson, E., Fortt, A., Iliescu, D., and Renshaw, C. (2006). "Failure envelope of first-year Arctic sea ice: The role of friction in compressive fracture". In: *Journal of Geophysical Research: Oceans* 111.C11.

Sodhi, D. S. (1977). *Ice arching and the drift of pack ice through restricted channels.* Vol. 77. 18. Department of Defense, Department of the Army, Corps of Engineers, Cold …

Timco, G. and Weeks, W. (2010). "A review of the engineering properties of sea ice". In: *Cold regions science and technology* 60.2, pp. 107–129.

Tran, H. D., Sulsky, D. L., and Schreyer, H. L. (2015). "An anisotropic elastic-decohesive constitutive relation for sea ice". In: *International Journal for Numerical and Analytical Methods in Geomechanics* 39.9, pp. 988–1013.

Tremblay, L. B. and Mysak, L. (1997). "Modeling sea ice as a granular material, including the dilatancy effect". In: *Journal of Physical Oceanography* 27.11, pp. 2342–2360.

Vihma, T. (2014). "Effects of Arctic sea ice decline on weather and climate: A review". In: *Surveys in Geophysics* 35.5, pp. 1175–1214.

Walker, D. (1966). "An approximate theory for pressures and arching in hoppers". In: *Chemical Engineering Science* 21.11, pp. 975–997.

Weiss, J., Schulson, E. M., and Stern, H. L. (2007). "Sea ice rheology from in-situ, satellite and laboratory observations: Fracture and friction". In: *Earth and Planetary Science Letters* 255.1-2, pp. 1–8.

West, B., O'Connor, D., Parno, M., Krackow, M., and Polashenski, C. (2022). "Bonded Discrete Element Simulations of Sea Ice With Non-Local Failure: Applications to Nares Strait". In: *Journal of Advances in Modeling Earth Systems* 14.6, e2021MS002614.

World Meterological Organization (1970). "WMO sea-ice nomenclature. Terminology, Codes and Illustrated Glossary." In: *WMD Publication* 259.

Eidesstattliche Versicherung

(Affidavit)

Bourgett, Mirjam Aline

Name, Vorname
(surname, first name)

202031

Matrikelnummer
(student ID number)

☐ Bachelorarbeit
   (Bachelor's thesis)

☑ Masterarbeit
   (Master's thesis)

Titel
(Title)

Implementation of a Maxwell Elasto-Brittle Rheology in a Sea Ice Model Coupled to an Ocean

Ich versichere hiermit an Eides statt, dass ich die vorliegende Abschlussarbeit mit dem oben genannten Titel selbstständig und ohne unzulässige fremde Hilfe erbracht habe. Ich habe keine anderen als die angegebenen Quellen und Hilfsmittel benutzt sowie wörtliche und sinngemäße Zitate kenntlich gemacht. Die Arbeit hat in gleicher oder ähnlicher Form noch keiner Prüfungsbehörde vorgelegen.	I declare in lieu of oath that I have completed the present thesis with the above-mentioned title independently and without any unauthorized assistance. I have not used any other sources or aids than the ones listed and have documented quotations and paraphrases as such. The thesis in its current or similar version has not been submitted to an auditing institution before.

Bremerhaven, 1.12.22

Ort, Datum
(place, date)

M. Bourgett

Unterschrift
(signature)

Belehrung:	Official notification:
Wer vorsätzlich gegen eine die Täuschung über Prüfungsleistungen betreffende Regelung einer Hochschulprüfungsordnung verstößt, handelt ordnungswidrig. Die Ordnungswidrigkeit kann mit einer Geldbuße von bis zu 50.000,00 € geahndet werden. Zuständige Verwaltungsbehörde für die Verfolgung und Ahndung von Ordnungswidrigkeiten ist der Kanzler/die Kanzlerin der Technischen Universität Dortmund. Im Falle eines mehrfachen oder sonstigen schwerwiegenden Täuschungsversuches kann der Prüfling zudem exmatrikuliert werden. (§ 63 Abs. 5 Hochschulgesetz - HG -).	Any person who intentionally breaches any regulation of university examination regulations relating to deception in examination performance is acting improperly. This offense can be punished with a fine of up to EUR 50,000.00. The competent administrative authority for the pursuit and prosecution of offenses of this type is the Chancellor of TU Dortmund University. In the case of multiple or other serious attempts at deception, the examinee can also be unenrolled, Section 63 (5) North Rhine-Westphalia Higher Education Act (*Hochschulgesetz, HG*).
Die Abgabe einer falschen Versicherung an Eides statt wird mit Freiheitsstrafe bis zu 3 Jahren oder mit Geldstrafe bestraft.	The submission of a false affidavit will be punished with a prison sentence of up to three years or a fine.
Die Technische Universität Dortmund wird ggf. elektronische Vergleichswerkzeuge (wie z.B. die Software „turnitin") zur Überprüfung von Ordnungs-widrigkeiten in Prüfungsverfahren nutzen.	As may be necessary, TU Dortmund University will make use of electronic plagiarism-prevention tools (e.g. the "turnitin" service) in order to monitor violations during the examination procedures.
Die oben stehende Belehrung habe ich zur Kenntnis genommen:	I have taken note of the above official notification:*

Bremerhaven, 1.12.22

Ort, Datum
(place, date)

M. Bourgett

Unterschrift
(signature)

*Please be aware that solely the German version of the affidavit ("Eidesstattliche Versicherung") for the Bachelor's/ Master's thesis is the official and legally binding version.